

UCSF

UC San Francisco Previously Published Works

Title

Mechanical Tension Promotes Formation of Gastrulation-like Nodes and Patterns Mesoderm Specification in Human Embryonic Stem Cells

Permalink

<https://escholarship.org/uc/item/5t61d46g>

Journal

Developmental Cell, 55(6)

ISSN

1534-5807

Authors

Muncie, Jonathon M
Ayad, Nadia ME
Lakins, Johnathon N
et al.

Publication Date

2020-12-01

DOI

10.1016/j.devcel.2020.10.015

Peer reviewed



Published in final edited form as:

Dev Cell. 2020 December 21; 55(6): 679–694.e11. doi:10.1016/j.devcel.2020.10.015.

Mechanical tension promotes formation of gastrulation-like nodes and patterns mesoderm specification in human embryonic stem cells

Jonathon M. Muncie^{1,2}, Nadia M.E. Ayad^{1,2}, Johnathon N. Lakins², Xufeng Xue³, Jianping Fu^{3,4,5}, Valerie M. Weaver^{2,6,7,8,9}

¹Graduate Program in Bioengineering, University of California San Francisco and University of California Berkeley, San Francisco, CA 94143, USA

²Center for Bioengineering and Tissue Regeneration, Department of Surgery, University of California San Francisco, San Francisco, CA 94143, USA

³Department of Mechanical Engineering, University of Michigan, Ann Arbor, MI 48109, USA

⁴Department of Biomedical Engineering, University of Michigan, Ann Arbor, MI 48109, USA

⁵Department of Cell and Developmental Biology, University of Michigan Medical School, Ann Arbor, MI 48109, USA

⁶Eli and Edythe Broad Center of Regeneration Medicine and Stem Cell Research, University of California San Francisco, San Francisco, CA 94143, USA

⁷UCSF Comprehensive Cancer Center, Helen Diller Family Cancer Research Center, University of California San Francisco, San Francisco, CA 94143, USA

⁸Department of Anatomy, Department of Bioengineering and Therapeutic Sciences, and Department of Radiation Oncology, University of California San Francisco, San Francisco, CA 94143, USA

⁹Lead Contact

Summary

Embryogenesis is directed by morphogens that induce differentiation within a defined tissue geometry. Tissue organization is mediated by cell-cell and cell-extracellular matrix (ECM)

*Correspondence: Valerie M. Weaver, 513 Parnassus Avenue, HSE 560, Box 0456, Department of Surgery, UCSF, San Francisco, CA 94143-0456, Telephone: 415-476-8562, valerie.weaver@ucsf.edu.

Author Contributions

Experimental Conceptualization: V.M.W., J.M.M., N.M.E.A., J.N.L., X.X., and J.F. Methodology: J.M.M., J.N.L., X.X., and J.F. Software: J.M.M. and N.M.E.A. Validation: J.M.M. and J.N.L. Formal Analysis: J.M.M. and N.M.E.A. Investigation: J.M.M., N.M.E.A., J.N.L., and X.X. Resources: V.M.W. and J.F. Writing – Original Draft: J.M.M. and V.M.W. Writing – Review & Editing: V.M.W., J.M.M., N.M.E.A., J.N.L., X.X., and J.F. Visualization: J.M.M., N.M.E.A., and X.X. Supervision: V.M.W., J.N.L., and J.F. Funding Acquisition: V.M.W.

Declaration of Interests

The authors declare no competing interests.

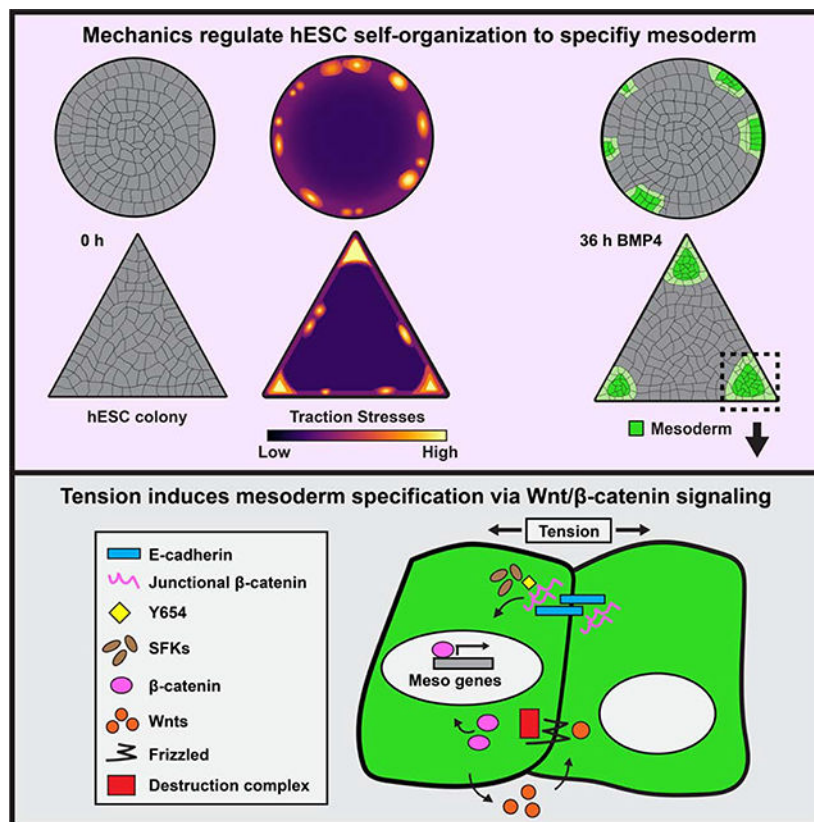
Publisher's Disclaimer: This is a PDF file of an unedited manuscript that has been accepted for publication. As a service to our customers we are providing this early version of the manuscript. The manuscript will undergo copyediting, typesetting, and review of the resulting proof before it is published in its final form. Please note that during the production process errors may be discovered which could affect the content, and all legal disclaimers that apply to the journal pertain.

adhesions and is modulated by cell tension and tissue-level forces. Whether cell tension regulates development by modifying morphogen signaling is less clear. Human embryonic stem cells (hESCs) exhibit an intrinsic capacity for self-organization, which motivates their use as a tractable model of early human embryogenesis. We engineered patterned substrates that recapitulate the biophysical properties of the early embryo and mediate the self-organization of “gastrulation-like” nodes in cultured hESCs. Tissue geometries that generated local nodes of high cell-adhesion tension directed the spatial patterning of the BMP4-dependent “gastrulation-like” phenotype by enhancing phosphorylation and junctional release of β -catenin to promote Wnt signaling and mesoderm specification. Furthermore, direct force application via mechanical stretching promoted BMP-dependent mesoderm specification, confirming that tissue-level forces can directly regulate cell fate specification in early human development.

In Brief

Muncie et al. develop engineered substrates that recapitulate the biophysical properties of the early embryo and facilitate “gastrulation-like” morphogenesis of hESCs. They demonstrate that specific tissue geometries foster localized regions of high cell-adhesion tension that potentiate BMP4-dependent mesoderm specification by enhancing junctional release of β -catenin to promote Wnt signaling.

Graphical Abstract



Keywords

Human embryonic stem cells; self-organization; gastrulation; mesoderm; polyacrylamide hydrogels; tissue patterning; cytoskeletal tension; traction force microscopy

Introduction

Gastrulation – wherein cells of the embryonic epiblast simultaneously segregate and differentiate into the three primary germ layers: ectoderm, mesoderm, and endoderm – requires precise coordination of morphogenesis and cell fate specification. The morphogenesis that occurs during gastrulation relies on cell tension and tissue-level forces to facilitate the physical re-organization of epiblast cells into the primary germ layers (Hamada, 2015; Ko and Martin, 2020; Paré and Zallen, 2020; Voiculescu et al., 2014; Williams and Solnica-Krezel, 2017). As embryogenesis progresses, tissue-level forces sculpt the embryo by driving neural tube closure, mediating somitogenesis, and guiding heart tube looping (McMillen and Holley, 2015; Ramasubramanian et al., 2013; Taber, 2014; Turlier and Maître, 2015; Vijayraghavan and Davidson, 2017). Thus, cell- and tissue-level forces play an intimate role in directing the structure and function of the emerging organism. Yet, whether these forces may directly influence cell fate specification during early embryogenesis by modifying cell signaling, transcription, and tissue-specific differentiation, and how, remains less well understood.

Remarkably, hESCs will self-organize to recapitulate patterns of the primary germ layers, even in the absence of extraembryonic tissues (Shao et al., 2017; Simunovic et al., 2019; Warmflash et al., 2014; Zheng et al., 2019). Prior studies using hESCs underscored the importance of tissue organization in early human development, and implicated morphogen gradients and receptor accessibility as two key mechanisms that regulate primary germ layer patterning (Blin et al., 2018; Chhabra et al., 2019; Etoc et al., 2016; Manfrin et al., 2019; Martyn et al., 2019; Smith et al., 2018; Tewary et al., 2019; Warmflash et al., 2014). The coordination of cellular contractility throughout many cells in multicellular tissues can give rise to tissue-level forces that are dependent on tissue organization. Cell-adhesion tension, in particular, is spatially enhanced by specific tissue geometries (Gomez et al., 2010; Kilian et al., 2010; Lee et al., 2016; Nelson et al., 2005). This raises the intriguing possibility that tissue geometry modulates local cell-adhesion tension to spatially direct hESC self-organization and fate specification.

Here we explored the role of cell-adhesion tension in the generation of spatially-patterned, “gastrulation-like” nodes in hESCs. We used hESCs cultured on geometrically-defined ECMs of tuned elasticity to recapitulate the biophysical properties of the early embryo and promote “gastrulation-like” morphogenesis. Using this system, and by applying mechanical stress via stretching, we implicated tension as an additional key regulator of cell fate patterning and determined that cell-adhesion tension promotes mesoderm specification by regulating Wnt/ β -catenin signaling. The findings reveal a direct relationship between cell-adhesion tension and morphogen-dependent differentiation, and emphasize the versatility of

hESCs as a tractable model to study how mechanics influence cell fate specification in early human development.

Results

Compliant substrates promote hESC self-organization into “gastrulation-like” nodes

To study the interplay between tissue mechanics and early development, we designed reproducible culture strategies that foster hESC self-organization and consistently permit a “gastrulation-like” phenotype following BMP4 stimulation. hESCs plated as confined circular colonies on ECM-patterned rigid glass substrates (Elastic modulus, $E = 10^9$ to 10^{10} Pa) exhibit a radial pattern of primary germ layer specification following BMP4 stimulation (Warmflash et al., 2014). This has been attributed to restriction of BMP/SMAD signaling to the margins of these colonies, combined with the presumptive role of endogenously secreted BMP inhibitors concentrated at the colony interior and consistent with a reaction-diffusion model (Etoc et al., 2016; Tewary et al., 2017). By contrast, hESCs plated at high densities (3,000–4,000 cells/mm²) using “funnels” on polyacrylamide hydrogels (PA; $E = 10^2$ to 10^5 Pa) modified with laminin-rich reconstituted basement membrane (rBM; Matrigel equivalent) self-assemble disc-shaped colonies and undergo enhanced mesoderm specification upon BMP4 stimulation when cultured on the soft ($E = 10^2$ to 10^3 Pa) versus the stiff ($E = 10^4$ to 10^5 Pa) substrates (L. Przybyla et al., 2016a; L. Przybyla et al., 2016b). Atomic force microscopy (AFM) measurements of the gastrulation-stage chicken epiblast, which resembles these hESC disc cultures in size and shape (Mikawa et al., 2004; Shahbazi et al., 2016), yielded values within the soft (10^2 to 10^3 Pa) elasticity range (Figure S1A–B). Thus, we developed a system for BMP4-induced differentiation on embryo-like compliant PA gels (Figure 1A). For technical reasons, we chose the softest PA gel condition that was experimentally compatible with both confined and unconfined culture methods ($E = 2,700$ Pa). Importantly, hESCs cultured on 2,700 Pa substrates and stimulated with BMP4 exhibited similar levels of mesoderm specification as on 400 Pa substrates (Figure S1C), which most closely recapitulate the elasticity of the chicken embryo (Figure S1B).

Live-imaging of H2B-mCherry-labelled nuclei following BMP4-mediated differentiation (50 ng/ml; 24 to 48 hours) revealed that multiple discrete regions of highly dense hESCs formed near the periphery of these unconfined colonies on soft hydrogels (Figures 1B, 1D, Video S1). High-magnification spinning disc confocal imaging of a subset of these colonies showed that the hESCs ingressed basally within the observed nodes to ultimately assemble into a second cellular layer that expressed the mesoderm marker T(brachyury) (Figures 1C and S1E). This cellular behavior is highly reminiscent of gastrulation, wherein cells of the developing epiblast ingress at the embryo midline to form a secondary transient structure called the primitive streak, which gives rise to the mesoderm and endoderm germ layers (Shahbazi et al., 2019; Shahbazi and Zernicka-Goetz, 2018; Simunovic and Brivanlou, 2017; Voiculescu et al., 2014; Williams and Solnica-Krezel, 2017). Analogous to the embryonic primitive streak that elongates as gastrulation progresses, these “gastrulation-like” nodes in the hESC colonies similarly continued to expand between 24 and 48 hours post-BMP4-stimulation (Figures 1E and S1D). Consistent with gastrulation, the hESCs that expressed T(brachyury) in “gastrulation-like” nodes also lost E-cadherin, indicating they had

undergone an epithelial to mesenchymal transition (EMT; Figure 1F). Indeed, the cells adjacent to the “gastrulation-like” nodes expressed another EMT marker, Slug, implying they were in the process of EMT and would subsequently undergo mesoderm specification as part of the expanding node (Figure 1G).

Cells within these “gastrulation-like” nodes also demonstrated a trend towards increased expression of fibronectin (FN1) and significant upregulation of key matrix metalloproteinases (MMPs) involved in remodeling the ECM during gastrulation, namely, MMP2 and MMP14 (Figure S1F; Kyprianou et al., 2020; Zhang et al., 2003). By 72 hours post-BMP4-stimulation, we observed deposition and fibrillogenesis of fibronectin within the “gastrulation-like” nodes (Figure S1G). These data provide evidence that the mesoderm-specified cells actively remodeled their ECM, likely to facilitate further ingression and migration of mesoderm progenitors, as in the embryo (Davidson et al., 2008; Keller, 2005; Kyprianou et al., 2020).

These findings illustrate our ability to reproducibly induce a “gastrulation-like” phenotype, indicative of early embryogenesis, in self-organized nodes of hESCs resembling the primitive streak that forms during gastrulation in the embryo (Figure 1H). The mesoderm specification that we observed in our model bears some similarity to the patterns documented in earlier studies (Etoc et al., 2016; Tewary et al., 2017; Warmflash et al., 2014), in that both systems result in mesoderm specification occurring near the colony periphery. However, the formation of discrete “gastrulation-like” nodes in unconfined hESC colonies on compliant PA gels is distinct from the apparent continuous concentric ring patterns of the primary germ layers observed on patterned glass substrates, and instead, each “gastrulation-like” node observed in our system is morphologically reminiscent of a discrete primitive streak. This distinction underscores the importance of recapitulating the biophysical properties of the local microenvironment in faithfully modeling self-organization of the early embryo.

Real-time monitoring of hESC “gastrulation-like” nodes

To explore the mechanisms regulating the self-organization that fosters the “gastrulation-like” phenotype in hESCs cultured on compliant substrates, we sought to monitor the temporal development of the nodes in real-time. We built a reporter cell line (T-reporter) with CRISPR homology-directed repair (HDR; Chu et al., 2015; San Filippo et al., 2008) to insert an mNeonGreen fluorophore into the endogenous TBXT gene, which encodes T(brachyury) (Figure 2A). We used a commercial antibody for T(brachyury) to validate that the T-reporter system effectively conveyed T expression levels following BMP4 stimulation (Figure 2B–C) and assessed additional fate specification markers of the cells in these “gastrulation-like” nodes (Figure 2D). Quantitative polymerase chain reaction (qPCR) revealed that the isolated T-positive hESCs expressed high levels of the mesoderm markers TBXT and GSC (goosecoid), and the EMT marker SNAI2, as compared to T-negative hESCs (Figure 2E). By contrast, T-negative hESCs expressed high levels of the pluripotent marker SOX2, excluding them from mesodermal identity (Figure 2E; Koch et al., 2017; Warmflash et al., 2014). Additionally, we found that direct transcriptional targets of T(brachyury) (Koch et al., 2017) were upregulated in the T-positive hESCs, verifying that

the T-mNeonGreen fusion protein did not compromise downstream transcriptional activity of T (Figure S2A–B). The data confirm that mesoderm specification occurs primarily in the observed “gastrulation-like” nodes, and indicate that the cells within these nodes undergo transcriptional changes akin to the cells that pass through the primitive streak during early gastrulation.

Time-course imaging of T-reporter hESC colonies following BMP4 stimulation revealed that the dynamic behavior of the entire tissue-like structure fosters the induction and expansion of the “gastrulation-like” nodes (Figure 2F; Videos S2, S3). Coincident with T-expression and emergence of the “gastrulation-like” phenotype, the hESCs approximately 50 microns or 10 cell diameters inward from the colony periphery (Figure S2C–D) begin to assemble into multiple densely packed aggregates (Figure 2F–G; Videos S2, S3). These densely packed cellular aggregates progressively increased in size (Figures 2H and S2C), presumably due to observed fluid-like collective movements that initially drive cells radially-outwards and then drive subpopulations back inward to contribute to the developing “gastrulation-like” nodes (Figure 2F; Videos S2–S4). These collective movements apparently mimic the “Polonaise” movements that drive epiblast cells toward the midline and establish the primitive streak in the gastrulating chicken embryo (Video S4; Voiculescu et al., 2014). These data thus provide additional compelling evidence that recapitulating the compliance of the embryo enables self-organization of hESCs to facilitate coordinated programs of early embryogenesis (Figure 1H).

Cell-adhesion tension directs “gastrulation-like” node organization to specify mesoderm

We previously showed that hESC colonies cultured on compliant hydrogels demonstrated a unique ability to generate regions of high tension near the periphery of colonies maintained in pluripotent conditions (L. Przybyla et al., 2016a). Traction force microscopy (TFM) measurements of hESC colonies were combined with monolayer stress microscopy to reveal that regions of high traction stresses corresponded to regions of high cell-adhesion tension. This can be explained by the epithelial structure of hESC colonies, which results in cell-cell tension being distributed through cellular adhesions and balanced by measurable cell-substrate stresses. Thus, we measured cell-adhesion tension using TFM prior to stimulation with BMP4 and used live-cell imaging of the T-reporter to register these forces with the “gastrulation-like” nodes that emerge following BMP4 stimulation. Remarkably, the “gastrulation-like” nodes developed within the same hESC colony regions that exhibited the highest cell-adhesion tension prior to differentiation (Figure 3A–B). The data imply that cell-adhesion tension may regulate spatial patterning of the “gastrulation-like” phenotype and could account for the unique formation of discrete nodes of mesoderm specification observed in our system, as compared to the continuous ring patterns previously reported (Etoc et al., 2016; Tewary et al., 2017; Warmflash et al., 2014).

To test the relationship between cell-adhesion tension and the “gastrulation-like” phenotype, we geometrically-confined hESC colonies on engineered compliant substrates designed to direct the localization of cell-adhesion tension (Muncie et al., 2019). After confirming that hESCs plated on the patterned substrates did not spontaneously differentiate (Figure S3A–C), we monitored the force-generating behavior of the hESC colonies. We determined that

specific tissue geometries previously shown to promote localized tension within an epithelial cell colony (Gomez et al., 2010; Kilian et al., 2010; Lee et al., 2016; Nelson et al., 2005; Smith et al., 2018) similarly induced high cell-adhesion tension in the hESC colonies maintained in pluripotent conditions. For instance, shapes such as squares and triangles fostered the highest cell-adhesion tension in the colony corners, whereas circles developed comparatively moderate levels of tension around their colony periphery (Figures 3C and S3D). As predicted, live-cell imaging of the T-reporter showed that following BMP4 stimulation, “gastrulation-like” nodes were initiated in the colony regions that displayed the highest cell-adhesion tension prior to differentiation, before mesoderm specification then spread throughout the colony periphery (Figures 3D and S3D; Video S5). The averaged intensity of multiple cell-adhesion tension and T-expression plots confirmed that the initiation of mesoderm specification detectable by 30 hours of BMP4 stimulation on compliant substrates did indeed consistently arise within colony regions that displayed high cell-adhesion tension prior to BMP4 addition (Figure 3E–F). By contrast, on highly rigid substrates we observed uniform initiation of mesoderm specification around the colony periphery, as previously reported (Figure S3E–F; Smith et al., 2018; Warmflash et al., 2014). Geometric confinement of hESC colonies on highly rigid substrates also leads to regional differences in local cell density that appear to pattern mesoderm specification (Blin et al., 2018). We noted that hESC colonies on compliant substrates exhibit nearly uniform cell density prior to BMP4 stimulation, with a slight drop in density within 50 μm from the colony edge, and that there is no apparent correlation between the distribution of cell density and the initiation of mesoderm specification (Figure S4A).

We next sought to differentiate between cell-adhesion tension and gradients of apically-secreted diffusible factors in hESC mesoderm specification. To facilitate a direct comparison of results with prior studies (Etoc et al., 2016; Tewary et al., 2017), we generated patterned substrates on tissue culture plastic. Our design consisted of a triangle colony positioned with one corner inside the “mouth” of a Pac-Man colony, separated by the smallest feasible gap between the two colonies that was large enough to prevent colony fusion and cell-adhesion tension transmission (75 μm ; Figure S4B). We rationalized that if BMP inhibitors were secreted apically and were concentrated in a radially expanding gradient that permits high BMP signaling at the periphery of the colony and represses signaling at the center, then the cells in the triangle corner within the “mouth” of the Pac-Man colony would be exposed to higher concentrations of inhibitory signals than the two distal corners. Thus, the distal corners would be expected to exhibit higher levels of mesoderm specification than the corner within the Pac-Man colony “mouth.” However, contrary to this prediction, we observed equivalent levels of mesoderm specification in all three corners (Figure S4B–C). This observation would be in line with previous models if the exogenous activator (BMP4) diffused through the gap between the Pac-Man and triangle colonies and overrode the endogenously secreted inhibitors; however, if this were the case, we would have also detected mesoderm specification within the “mouth” of the Pac-Man colony. Instead, we found mesoderm specification was excluded from the edge inside the “mouth” of the Pac-Man colony (Figure S4B–C). Thus, the findings indicate that gradients of activators and inhibitors are not likely the sole factors directing cell fate patterning, and rather, suggest

that the measured regions of cell-adhesion tension co-regulate mesoderm specification in these hESC colonies.

Cell-cell adhesion mediates the high tension required to develop “gastrulation-like” nodes

To further explore the role of cell-adhesion tension in hESC colony self-organization and “gastrulation-like” node formation, we attenuated cell-cell adhesions by knocking down E-cadherin (encoded by CDH1 gene) and examined the effect on mesoderm specification. Inducible short hairpin RNA knockdown that achieved a 50 percent reduction in CDH1 (shCDH1; Figure 4A–C) was sufficient to significantly reduce the magnitude of cell-adhesion tension in the triangle hESC colonies, relative to control colonies, which was particularly evident in the colony corners (Figure 4D–E, Figure S5). This level of E-cadherin knockdown and the reduced cell-adhesion tension also significantly decreased the level of mesoderm specification observed in the hESC colonies (Figure 4F–G). The findings indicate that cell-cell adhesion, mediated by structural proteins such as E-cadherin, is necessary for the spatially-organized regions of high cell-adhesion tension that, in turn, promote mesoderm specification in hESC colonies.

Ablating regions of high cell-adhesion tension inhibits, whereas mechanical stretching promotes mesoderm specification

To more definitively establish the roles of tissue organization and cell-adhesion tension in mesoderm specification, we directly ablated tension in patterned colonies of hESCs. We generated precise cuts across the corners of the triangle hESC colonies using an eyebrow knife (Sive et al., 2000), which disrupted the spatially-restricted regions of high cell-adhesion tension (Figure 5A–B). Consistent with our assertion that localized regions of high cell-adhesion tension direct the “gastrulation-like” nodes that promote mesoderm specification, we noted a significant delay in BMP4-induced T-reporter expression in the cut corners of these colonies (Figure 5C–D).

Due to the fact that physically ablating hESC colonies may have produced confounding effects that delayed mesoderm specification, we sought further evidence of a causal link between localized cell-adhesion tension and the development of “gastrulation-like” nodes. We thus designed Pac-Man patterned surfaces that generated low cell-adhesion tension at the concave edge of the hESC colony, corresponding to the “mouth” of the Pac-Man (Figure 5E–F). We consistently observed contraction of Pac-Man colonies (especially the “mouth” vertices) between the time of BMP4 addition and detection of T-reporter expression, explaining the appearance of T-reporter expression slightly internalized from the regions of high cell-adhesion tension prior to BMP4-stimulation (Figure 5F–G). Although T-reporter expression was consistently induced around the high-tension convex edges of the Pac-Man, T-reporter expression was clearly excluded from the low-tension concave edge of the “mouth” (Figure 5E–G). The results provide support for our assertion that high cell-adhesion tension directs the spatial localization of “gastrulation-like” nodes that specify mesoderm in hESC colonies on compliant substrates.

We next tested whether cell-adhesion tension is sufficient to induce mesoderm specification. Colonies of hESCs were cultured on flexible PDMS microdevices that subjected the low-

tension, central region of circular colonies to mechanical stress via prolonged stretching (Figure 5H; Xue et al., 2018). Consistent with our prediction, mechanical stretch induced BMP-dependent mesoderm specification within the otherwise low-tension central colony region (Figure 5I–J). The data indicate that tension, per se, can collaborate with BMP signaling to drive mesoderm specification in hESCs, even in colony regions exposed to high concentrations of endogenously secreted inhibitory signals (Etoc et al., 2016; Tewary et al., 2017).

High tension promotes β -catenin release from adherens junctions to specify mesoderm

Mesoderm specification in hESC colonies depends on Wnt/ β -catenin signaling and is enhanced by growth on a compliant matrix (L. Przybyla et al., 2016b). Accordingly, we examined whether localized cell-adhesion tension specifies mesoderm by promoting the release of β -catenin from E-cadherin adhesion complexes, specifically in regions of high tension. We observed the preferential loss of β -catenin from E-cadherin junctions within the localized regions of high cell-adhesion tension 24 hours following BMP4 stimulation (Figure 6A–B). Activated phospho-Src-family kinases (pSFKs) phosphorylate junctional β -catenin to facilitate its release from adherens junction complexes (Bienz, 2005; Gayrard et al., 2018; Gottardi and Gumbiner, 2004; Howard et al., 2011; Lilien and Balsamo, 2005; L. Przybyla et al., 2016b). We detected high levels of pSFKs within 6 hours of BMP4 stimulation, specifically within regions of high cell-adhesion tension (Figures 6C and S6). Blocking pSFK activity, using the Src inhibitor PP1, prevented β -catenin release at the E-cadherin junctions within the regions of high tension (Figure 6C–E). Furthermore, preventing β -catenin release via Src inhibition resulted in a significant loss of mesoderm specification, as indicated by decreased TBXT, GSC, and SNAI2 expression, and elevated SOX2 levels (Figure 6F).

Molecular dynamic simulations showed tension across E-cadherin junctions exposes the tyrosine 654 (Y654) of cadherin-bound β -catenin (Röper et al., 2018). Therefore, we asked whether high cell-adhesion tension fosters a conformational change in β -catenin that permits its phosphorylation on Y654 to spatially pattern mesoderm specification at the nodes of high tension. We detected enhanced binding of an antibody specific to the β -catenin Y654 in the cells at the corners of the triangle hESC colonies, as well as at the convex edges of Pac-Man colonies, suggesting the higher cell-adhesion tension in these regions exposed the Y654 phosphorylation site (Figure 6G–H). The data demonstrate that the structure of junctional β -catenin is physically modified by cell-adhesion tension, that the release of junctional β -catenin is regulated by pSFKs, and that the subsequent availability of β -catenin for nuclear translocation and transcriptional activity initiates mesoderm specification in regions of high tension (Figure 6I).

Wnt signaling reinforces mesoderm specification in regions of high tension

To determine whether canonical Wnt/ β -catenin signaling is involved in promoting mesoderm specification following its initiation in regions of high cell-adhesion tension, we used FACS to isolate T-positive cells from geometrically-confined hESC colonies following BMP4 stimulation (36 h; subsequent to junctional β -catenin release), and evaluated Wnt ligand expression (Figure 7A). Gene expression analysis revealed that the canonical Wnt

ligands WNT3A and WNT8A, which are critical for mesoderm specification (Chhabra et al., 2019; Kemp et al., 2005; Lindsley et al., 2006; Martyn et al., 2019; L. Przybyla et al., 2016b), were expressed at higher levels in the T-positive cells isolated from the regions of high cell-adhesion tension (Figure 7B). By contrast, levels of the non-canonical ligand WNT4 were higher in the isolated T-negative cells (Figure 7B). Moreover, blocking Wnt ligand processing and secretion with the inhibitor IWP-2 (2 μ M) resulted in a significant loss of mesoderm specification, as indicated by decreased TBXT, GSC, and SNAI2 expression, and elevated SOX2 levels (Figure 7C).

In situ hybridization via hybridization chain reaction (ISH-HCR; Choi et al., 2018) verified that WNT3A transcription was upregulated in response to BMP4 within the same high-tension colony regions (Figure 7D–E, Figure S7). Moreover, because blocking SFK activity with PP1 prevented upregulation of the mesoderm-inducing Wnts, Src-mediated release and transcriptional activity of β -catenin appears to be necessary for tension-regulated Wnt ligand expression (Figure 7F–H). Collectively, the findings elucidate a two-part mechanism whereby high cell-adhesion tension initiates a spatially-restricted, Src-mediated release of β -catenin from adherens junctions, which then feeds forward to drive canonical Wnt signaling that promotes further mesoderm specification to reinforce the “gastrulation-like” phenotype (Figure 7I).

Discussion

It has long been recognized that mechanical forces are necessary to drive morphogenesis (Hamada, 2015; Ko and Martin, 2020; Paré and Zallen, 2020; Voiculescu et al., 2014; Williams and Solnica-Krezel, 2017), and we provide compelling evidence that these same forces influence cell fate specification by modifying the cellular response to morphogen signaling. Specifically, we demonstrate that mechanics alters BMP4-mediated patterning of hESCs by spatially promoting junctional release of β -catenin in regions of high-cell adhesion tension, which feeds forward to drive Wnt ligand expression. Notably, Wnt/ β -catenin signaling is conserved among model organisms and plays multiple roles throughout the course of embryogenesis and in adult stem cells (Clevers, 2006; Eliazer et al., 2019; Petersen and Reddien, 2009; van Amerongen and Nusse, 2009), implying that the tension-regulated activation of the pathway that we illustrate here is likely also conserved and re-used throughout development. In fact, Farge and colleagues demonstrated that the same Src-mediated phosphorylation at Y654 and subsequent release of junctional β -catenin occurs during mesoderm invagination in both zebrafish and *Drosophila* embryos (Brunet et al., 2013; Röper et al., 2018). A recent study of the tissue-level forces underlying gastrulation in avian embryos revealed that higher contractile forces are generated at the posterior of the embryo, in the margin between the epiblast and extraembryonic tissue (Saadaoui et al., 2020). We propose that the contractile forces identified by Saadaoui et al., in combination with presumed forces transduced across cell junctions as epiblast cells are pulled towards the midline, act to mechanically stretch and expose β -catenin Y654 to initiate the signaling cascade that leads to synchronized ingression and mesoderm specification at the primitive streak. Our findings illustrate a critical interplay between the mechanics that drive tissue development and the molecular signaling that regulates cell fate specification.

Prior studies illustrated that variations in BMP receptor accessibility and secreted morphogen concentrations lead to patterning of mesoderm specification within a concentric ring inwards from the hESC colony edge (Chhabra et al., 2019; Etoc et al., 2016; Manfrin et al., 2019; Martyn et al., 2019; Tewary et al., 2019, 2017; Warmflash et al., 2014). Our studies expand upon these findings to suggest that colonies of hESCs cultured on compliant substrates are particularly useful for studying the physical and molecular regulators of early embryogenesis, because they self-organize discrete “gastrulation-like” nodes that expand radially, distinctly resembling the formation and elongation of the primitive streak in the developing embryo (Mikawa et al., 2004; Voiculescu et al., 2014). It is possible that the formation of multiple “gastrulation-like” nodes in hESC colonies on compliant substrates, compared to a single primitive streak in the embryo, could be attributed to the lack of extraembryonic tissues in our system, which provide inhibitory signals to spatially restrict primitive streak formation to a single region at the posterior of the embryo (Bertocchini and Stern, 2002).

Previous work in 2D *in vitro* systems suggested that mesoderm specification of mouse ESCs occurs at regions of low local cell density (Blin et al., 2018); however, studies in the chicken embryo suggest that primitive streak formation occurs in regions of higher cell density (Lee et al., 2020; Spratt and Haas, 1960). Our analysis of cell density in hESC colonies reveals that there is no clear correlation between local density and the observed patterns of mesoderm specification. Additional studies are needed to understand precisely how cell density might regulate cell fate specification, perhaps by altering signaling, as suggested for contact-mediated patterning in 3D embryoid bodies (Sagy et al., 2019).

To address the role of endogenously secreted factors in our system, we positioned triangle colonies with one corner inside the mouth of Pac-Man colonies, and showed that mesoderm specification arises in the triangle corner positioned in the mouth at the same levels observed in the distal corners. This finding, together with our observation that T(brachyury) expression arises in the corners of triangle colonies on compliant substrates, rather than uniformly around the periphery as has been reported for colonies on rigid substrates, suggests that mesoderm specification is indeed co-regulated by the cell-adhesion tension developed in the colonies when they are cultured on compliant substrates, and not strictly determined by morphogen gradients alone. While this should not be taken as evidence to diminish the role of endogenously secreted factors, it constrains the models of inhibitor diffusion that are likely to pattern fate specification. A gradient arising from apical secretion should not have been significantly affected by the gap between triangle and Pac-Man colonies; thus, the result argues that inhibitor diffusion via the basal intercellular space, which is spatially constrained by the apical junctional complex (AJC), is much more likely to be involved in fate patterning. Future studies should be aimed at understanding how mechanical cues and signaling gradients are integrated to determine cell fate.

Remarkably, ESCs aggregated in 3D undergo key aspects of early embryogenesis, including germ layer specification, axial organization, elongation, expression of Hox genes, and somitogenesis (Beccari et al., 2018; Harrison et al., 2017; Sozen et al., 2018; van den Brink et al., 2020; Van Den Brink et al., 2014). In our pseudo-2D system, we are limited to observing the initial events of gastrulation, namely, coordinated morphogenesis akin to

“Polonaise” movements and ingression of mesoderm progenitors. Studies that implement tools such as molecular force sensors are needed to investigate the role of cell-adhesion tension in the later events of axial mesoderm/definitive endoderm segregation and somitiogenesis, which apparently occur exclusively in 3D models. Nevertheless, the observed similarities between the dynamics of “gastrulation-like” node formation in pseudo-2D hESC colonies on compliant substrates and embryonic primitive streak morphogenesis are striking. Thus, this system could prove to be a powerful model with which to dissect the interplay between tissue-level forces, cell-adhesion tension, and the signaling and transcriptional programs that regulate early human embryogenesis.

STAR METHODS

RESOURCE AVAILABILITY

Lead Contact—Further information and requests for resources and reagents should be directed to and will be fulfilled by the Lead Contact, Valerie M. Weaver (valerie.weaver@ucsf.edu).

Materials Availability—Modified plasmids and CAD drawings for 3D-printed parts can be made available upon request.

Data and Code Availability—The code generated during this study for analysis and visualization of traction force microscopy data is publicly available on GitHub: https://github.com/jmmuncie/TF_hESC.

EXPERIMENTAL MODELS AND SUBJECT DETAILS

Cell Lines—Human embryonic stem cells (parental line H9, female) were obtained as a gift from the Laboratory of Susan Fisher at UCSF and maintained in a humidified incubator at 37 °C with 5% CO₂. T-mNeonGreen, H2B-mCherry, and shCDH1 lines were all generated from H9s, as detailed in the subsequent sections of the Method Details.

T-mNeonGreen reporter cells were maintained on γ -irradiated primary mouse embryonic fibroblasts (PMEFs) in KSR media consisting of knockout-DMEM (Gibco) with 20% knockout serum replacement (Gibco), 2 mM L-glutamine (Gibco), 1 mM non-essential amino acids (Gibco), 1 \times antibiotic-antimycotic (Gibco), 100 μ M β -mercaptoethanol, supplemented with 10 ng/ml bFGF (PeproTech), and passaged with collagenase type IV (Gibco) at 1 mg/ml in knockout-DMEM (Gibco). PMEFs, derived from CF-1 mice, were obtained as a gift from the Laboratory of Susan Fisher at UCSF and were cultured in a humidified hypoxic incubator at 37 °C with 5% O₂ and 5% CO₂ on tissue culture plastic coated with 0.1% gelatin (Sigma) and in media consisting of DMEM, high glucose, with L-glutamine and sodium pyruvate (GenClone) supplemented with 10% fetal bovine serum (HyClone), 4 mM L-glutamine (Gibco), 1 \times antibiotic-antimycotic (Gibco), 10 ng/ml insulin (Roche), 20 ng/ml transferrin (Sigma), and 30 nM sodium selenite (VWR). PMEFs were γ -irradiated with a total dose of 40 Gy to induce mitotic arrest and frozen aliquots were stored in liquid nitrogen prior to being thawed and plated onto tissue culture plastic coated with 0.1% gelatin (Sigma) for passaging of T-mNeonGreen reporter cells.

H9, H2B-mCherry, and shCDH1 lines were maintained in feeder-free conditions on tissue culture plastic coated with reconstituted basement membrane extract (rBM; Matrigel equivalent; R&D Systems) in media consisting of 50% PMEF-conditioned KSR media and 50% complete Essential 8 media (E8; Gibco), supplemented with 10 ng/ml bFGF (PeproTech). PMEF-conditioned KSR media was generated by plating γ -irradiated PMEFs on tissue culture plastic coated with 0.1% gelatin (Sigma), feeding with KSR media supplemented with 4 ng/ml bFGF (PeproTech), and collecting and replacing the media every 24 h for 10–14 days. Cells in feeder-free conditions were passaged with 0.5 mM EDTA (Fisher) in PBS and plated into media supplemented with 10 μ M Y-27632 (ROCK inhibitor; Tocris) to promote survival. After 24 h, media was replaced with media lacking Y-27632.

The human embryonic kidney (HEK) 293T cell line, obtained as a gift from the Laboratory of Warren Pear at UPenn, was used for transfection and production of lentivirus, and was maintained in a humidified incubator at 37 °C with 5% CO₂. HEK 293T cells were cultured in DMEM, high glucose, with L-glutamine and sodium pyruvate (GenClone) supplemented with 10% fetal bovine serum (HyClone), 4 mM L-glutamine (Gibco), and 1 \times antibiotic-antimycotic (Gibco), and upon reaching 75% confluency, were passaged with 0.05% trypsin-EDTA (Gibco).

All cell lines were routinely tested and confirmed to be negative for mycoplasma contamination. All experiments involving hESCs were approved by the University of California San Francisco Human Gamete, Embryo and Stem Cell Research Committee (UCSF GESCR) study number 11–05439.

METHOD DETAILS

Generation of T-mNeonGreen reporter—H9 hESCs expressing a C-terminal fusion of the T-box transcription factor T (TBXT) gene [T(brachyury)] with the mNeonGreen fluorophore were prepared by CRISPR-Cas9 facilitated homology-directed repair (HDR). Guide RNAs (gRNAs) directing CRISPR-Cas9 double stranded cleavage near the end of the coding sequence of the human TBXT gene were cloned into a modified derivative of pX330-U6-Chimeric_BB-CBh-hSpCas9 (Addgene; modification: Lakins et al., in preparation) and screened for activity using the Surveyor Assay (Transgenomics) following transient transfection in HEK 293T cells. The gRNA with target sequence 5' - GCCTTGCTGCTTCACATGGA - 3' demonstrated the best activity and was cloned into a second modified version of pX330 for use in H9 cells, which we call SpCas9 U6 gRNA (Lakins et al., in preparation). Briefly, this derivative features gRNA under control of the U6 promoter as in pX330, a T2A polyprotein of SpCas9 and the human RAD51 gene under transcriptional control of the tetracycline-regulated TetO heptamerized minimal CMV promoter, an expression cassette for the advanced reverse tetracycline transcriptional transactivator rtTA^S-M22 (Urlinger et al., 2000), and the origin of replication from Epstein-Barr virus (OriP). For the targeting construct, approximately 1,000 base pairs upstream and downstream of the CRISPR-Cas9 cleavage site/TBXT gene stop codon was prepared by Long Range PCR using a Vent-Tth Polymerase mix (Sigma; New England BioLabs; Cheng et al., 1994) and cloned into pBluescript II KS⁺ (Stratagene) modified by the addition of OriP. This targeting construct was further modified by silent mutation of the gRNA targeting

sequence, removal of the natural TBXT gene stop codon, and insertion of a 22 amino acid glycine/serine/alanine rich flexible linker N-terminal to mNeonGreen in frame with the TBXT gene coding sequence. Following mNeonGreen, the construct included a Floxed expression cassette containing an mCherry fluorophore for assessing transfection efficiency and the puromycin resistance gene for selection of stably transfected cells.

H9 cells were co-transfected via electroporation with the described targeting construct, the SpCas9 U6 gRNA, and an *in vitro* transcribed capped, polyadenylated mRNA for the Epstein-Barr virus nuclear antigen 1 (EBNA-1) lacking the GA rich domain (Howden et al., 2006; targeting construct and SpCas9 U6 gRNA: Lakins et al., in preparation). Transfected H9s were re-plated on rBM-coated dishes in the presence of 10 μ M Y-27632 (Tocris) to promote survival and 1 μ g/ml of Doxycycline to induce the targeted CRISPR-Cas9 double-stranded break and subsequent homology-directed repair. Doxycycline was removed after 24 h and cells were allowed to recover an additional 24 h before selection with 0.25 μ g/ml of puromycin. Following selection, individual surviving colonies were mechanically passaged into separate wells, expanded, and then screened for gene targeting via Long Range PCR of genomic DNA using one primer anchored in mNeonGreen and a second in the TBXT gene upstream of the end of the 5' homology arm. Positive clones were expanded and subsequently transiently transfected with a plasmid expressing an EGFP-Cre fusion to remove the puromycin selection cassette. Transfected cells were FACS-sorted for EGFP expression 24 h later, re-plated in rBM-coated dishes in the presence of 10 μ M Y-27632, and following outgrowth of individual colonies, mechanically passaged into separate wells and screened by PCR for loss of the expression cassette. These cells were then characterized for expression of nuclear mNeonGreen expression following BMP4 differentiation, and verified by the concordance of mNeonGreen expression and detection of T(brachyury) by immunostaining.

Generation of H2B-mCherry—To generate the hESC line with fluorescent H2B-mCherry-labelled nuclei, an N-terminal fusion of human histone H2B to mCherry, under control of the human phosphoglycerate kinase promoter, was cloned into a transfer vector for transfection into HEK 293T cells, along with packaging and envelope vectors for self-inactivating transgenic lentivirus production, and subsequent transduction into H9s. Twenty-four hours prior to transfection, HEK 293T's were plated at a density of 0.8×10^6 cells into a 35 mm tissue culture plastic dish. The next day, HEK 293T's were washed once with PBS very gently to remove serum, and media was replaced with Opti-MEM (Gibco). To begin transfection, 1 μ g of total DNA consisting of 0.33 μ g psPAX2 packaging vector (Addgene), 0.16 μ g pMD2.G envelope vector (Addgene), and 0.55 μ g H2B-mCherry transfer vector was mixed with Opti-MEM media to a total volume of 100 μ L and incubated for 5 min at room temperature. Simultaneously, 3 μ g of polyethylenimine (PEI; Sigma) was mixed with 100 μ L Opti-MEM media and incubated for 5 min at room temperature. Following incubation, these two solutions were combined and incubated an additional 15 min at room temperature before being added to HEK 293T's. Six hours following transfection, media was replaced for normal HEK 293T growth media. Forty-eight hours post-transfection, viral supernatant was collected, cell debris was removed with 2×5 min centrifugation at $500 \times g$, carefully collecting supernatant and discarding pellets each time, and polybrene (Sigma) was added to

the final supernatant at 4 $\mu\text{g}/\text{ml}$. H9s plated on rBM-coated tissue culture plastic were immediately transduced by mixing viral supernatant 1:4 with E8 media (Gibco) supplemented with 10 ng/ml bFGF (PeproTech) and culturing cells in this media for 24 h, after which the media was replaced with fresh media and cultured for an additional 48 h. A pure population of cells expressing H2B-mCherry-labelled nuclei was obtained in two steps: first by enrichment via several rounds of mechanically picking morphologically undifferentiated colonies containing mCherry-positive cells and passaging as colony fragments onto γ -irradiated PMEFs, and then subsequently by FACS to purify. Single cells isolated by FACS were plated onto rBM-coated tissue culture plastic in E8 media (Gibco) supplemented with 10 ng/ml bFGF (PeproTech) and 10 μM Y27632 (Tocris) to promote survival. Fresh media was added every 24 h and Y27632 was reduced to 5 μM , 2.5 μM , and 0 μM on successive days, after which self-supporting undifferentiated colonies were obtained.

Generation of shCDH1—We utilized the same inducible shCDH1 hESC line from our previous work (L. Przybyla et al., 2016b). To generate the hESC line with inducible short hairpin RNA (shRNA) knockdown of CDH1, candidate shRNA hairpins were cloned into a transfer vector for transfection into HEK 293T cells along with packaging and envelope vectors for transgenic lentivirus production and subsequent transduction into H9s. The transfer vector consisted of a modified pLKO.1 neo plasmid (Addgene) with expression of the shRNA sequences under control of 3x copies of the lac operator, and contained a copy of the mNeonGreen fluorophore to assess transfection efficiency. The successful CDH1 shRNA had the following sequence: 5' - GAACGAGGCTAACGTCGTAAT - 3'. Transgenic lentivirus was produced in HEK 293T's as described in the preceding section for generation of the H2B-mCherry line. H9s plated on rBM-coated tissue culture plastic were immediately transduced by mixing viral supernatant 1:4 with E8 media (Gibco) supplemented with 10 ng/ml bFGF (PeproTech) and culturing cells in this media for 24 h, after which the media was replaced with fresh media and cultured for an additional 24 h, prior to selection with 200 $\mu\text{g}/\text{ml}$ G-418 (Sigma). shCDH1 cells were maintained with 200 $\mu\text{g}/\text{ml}$ G-418 prior to seeding for experiments to prevent loss of inducible CDH1 knockdown. CDH1 knockdown was induced with 200 μM isopropyl- β -D-thiogalactoside (IPTG; Sigma) added to the media one passage (72 h) prior to seeding on hydrogels.

Atomic Force Microscopy—Embryos were dissected from fertilized chicken eggs (Petaluma Farms) and cultured on top of filter paper to maintain tension across the blastoderm and vitelline membranes (Chapman et al., 2001) until Hamburger and Hamilton (HH) stage 3+ to 4, when the primitive streak is fully formed and mesodermal cells are actively ingressing (Hamburger and Hamilton, 1992; Voiculescu et al., 2014). Gastrulation-stage embryos were then mounted onto glass slides and placed on the stage of an MFP3D-BIO inverted optical AFM (Asylum Research) on a Nikon TE2000-U inverted microscope. Indentations were made using silicon nitride cantilevers with spring constants ranging from 0.05 to 0.07 N/m and borosilicate glass spherical tips 5 μm in diameter (Novascan Tech). The cantilevers were calibrated using the thermal oscillation method prior to each experiment. Embryos were indented at rates ranging from 0.75 to 1.25 $\mu\text{m}/\text{s}$ with a maximum force of 4.5 nN. The Hertz model was applied to the force curves obtained from

each indentation to calculate the elastic modulus (Young's modulus, stiffness). Embryos were assumed to be incompressible; therefore, a Poisson's ratio of 0.5 was used in the calculation of the elastic modulus.

Fabrication of Non-patterned Hydrogels—Polyacrylamide hydrogels were fabricated as described previously (Lakins et al., 2012; L. Przybyla et al., 2016a). First, #1 18 mm glass coverslips (Electron Microscopy Sciences) were modified with glutaraldehyde to promote attachment of polyacrylamide during polymerization. Coverslips were submerged in 0.2 M HCl (Fisher) overnight with gentle shaking, washed with ultrapure water, submerged in 0.1 M NaOH (Fisher) for 1 h with gentle shaking, washed with ultrapure water, submerged in a 1:200 dilution of 3-aminopropyltrimethoxysilane (Acros Organics) in ultrapure water for 1 h with gentle shaking, washed with ultrapure water, and finally submerged in a 1:140 dilution of 70% glutaraldehyde (Electron Microscopy Sciences) in PBS for 1 h with gentle shaking, washed with ultrapure water, and dried. Polyacrylamide solutions yielding the desired elastic moduli (E) were prepared and pipetted onto glutaraldehyde-modified coverslips with custom-made plastic spacers of approximately 100–200 μm thickness. For hydrogels of E = 400 Pa, the polyacrylamide solution consisted of 3% acrylamide (Bio-Rad), 0.05% Bis-acrylamide (Bio-Rad), 1x PBS, 1% TEMED (Bio-Rad) and 1% potassium persulfate (Sigma). For hydrogels of E = 2,700 Pa, the polyacrylamide solution consisted of 7.5% acrylamide (Bio-Rad), 0.035% Bis-acrylamide (Bio-Rad), 1x PBS, 1% TEMED (Bio-Rad) and 1% potassium persulfate (Sigma). A Rain-X-coated (Rain-X) coverslip was placed atop each glutaraldehyde-modified coverslip with polyacrylamide solution to form a polyacrylamide “sandwich”, and these were incubated for 1 h at room temperature to allow polymerization. The Rain-X coverslips and plastic spacers were then removed and the glutaraldehyde-modified coverslips with attached polyacrylamide gels were placed into custom 3D-printed holders (CAD drawings available upon request) with rubber gaskets to form sealed wells with the polyacrylamide hydrogels at the bottom of each well.

Next, the surfaces of the polyacrylamide gels were functionalized with N-succinimidyl acrylamido hexanoic acid (N6) to enable ECM ligands to bind to the surface and promote cell attachment. N6 was synthesized in a two-step process: first, condensation of acryloyl chloride and 6-aminohexanoic acid is performed to generate a 6-acrylamido hexanoic acid intermediate; second, this intermediate is isolated and dehydrated with NHS ester via a carbodiimide generated O-acylisourea to yield the final N6 product that is extracted and purified by crystallization (Lakins et al., 2012). A solution consisting of 50 mM HEPES (Fisher), pH 6.0, 0.01% Bis-acrylamide (Bio-Rad), 25% ethanol, 0.01% N6 (custom-synthesized), 0.002% Di(trimethylolpropane) tetraacrylate (Sigma), and 0.025% Irgacure D-2959 (Sigma) was prepared, pipetted into each well containing a polyacrylamide gel, and exposed for 10 min with a medium-wavelength UV source (Spectroline EN-180, 306 nm peak). The gels were then washed 2 \times 10 min with ice-cold 25 mM HEPES (Fisher), pH 6.0 and 2 \times 10 min with ice-cold 0.9% NaCl (Fisher). rBM was diluted to a concentration of 250 $\mu\text{g}/\text{ml}$ in ice-cold 100 mM HEPES (Fisher), 100 mM NaCl (Fisher), pH 8.0, added to each well containing a gel, and incubated at 4 $^{\circ}$ C overnight with gentle rocking. The gels were then washed 5 \times 10 min with PBS and stored at 4 $^{\circ}$ C in sterile conditions with PBS prior to beginning experiments.

Fabrication of Patterned Hydrogels—Patterned polyacrylamide hydrogels were fabricated as described previously (Muncie et al., 2019). Glutaraldehyde-modified coverslips were generated as described in the previous section for non-patterned hydrogels. Additional #1 18 mm coverslips (Electron Microscopy Services) were cleaned by overnight submersion in 1 M HCl (Fisher) with gentle rocking. Custom silicon wafers containing desired geometric patterns were generated using negative photoresist according to manufacturer's instructions (SU-8; Kayaku Advanced Materials, Inc.). Polydimethylsiloxane (PDMS; Dow) stamps with desired patterns were then fabricated on these custom silicon wafers. Stencils were generated by placing these PDMS stamps onto flat slabs of PDMS, wicking a UV-curable adhesive NOA-74 (Norland Products, Inc.) between the stamps and the flat slabs, and curing the adhesive via 10 min exposure with a medium-wavelength UV source (Spectroline EN-180, 306 nm peak). Next, stencils were firmly pressed onto the acid-washed coverslips and incubated overnight at 4° C with 250 µg/ml rBM in ice-cold 100 mM HEPES (Fisher), 100 mM NaCl (Fisher), pH 8.0. Stencils were then removed from the patterned coverslips and the coverslips were washed by two sequential submersions in PBS and a single submersion into ultrapure water before being dried under nitrogen gas (Airgas).

Polyacrylamide gels were then fabricated as described in the preceding section, with polyacrylamide solution being pipetted onto a glutaraldehyde-modified coverslip with plastic spacer and a patterned coverslip being placed on top, with the rBM-patterned side in contact with the polyacrylamide. These polyacrylamide “sandwiches” were incubated for 1 h at room temperature to allow polymerization, then submerged in PBS and incubated at room temperature with gentle rocking for an additional 2 h. The patterned top coverslips were removed using a scalpel while the “sandwich” remained submerged in PBS, and then the glutaraldehyde-modified coverslips with attached polyacrylamide gels were assembled into custom 3D-printed holders (CAD drawings available upon request) with rubber gaskets to form sealed wells with the polyacrylamide hydrogels at the bottom of each well. The gels were then washed 5× 10 min with PBS and stored at 4° C in sterile conditions with PBS prior to beginning experiments.

Micropatterning of Tissue Culture Plastic—Custom silicon wafers containing desired geometric patterns were generated using negative photoresist according to manufacturer's instructions (SU-8; Kayaku Advanced Materials, Inc.). Polydimethylsiloxane (PDMS; Dow) stamps with desired patterns were then fabricated on these custom silicon wafers. The stamps were then incubated overnight at 4° C with 250 µg/ml rBM in ice-cold 100 mM HEPES (Fisher), 100 mM NaCl (Fisher), pH 8.0. The next day, stamps were dried under nitrogen gas (Airgas), inverted and pressed onto the surface of tissue culture plastic 12-well plates, and incubated for 30 min at 37° C. Stamps were then removed and the wells were incubated at room temperature for 90 min with 1% BSA (Fisher), PBS. The BSA/PBS solution was removed and plates were stored at 37° C with knockout-DMEM (Gibco) prior to cell seeding.

Traction Force Microscopy—Polyacrylamide hydrogels were fabricated as described in the preceding sections and in previous work (Lakins et al., 2012; L. Przybyla et al., 2016a), with 1 µm diameter fluorescent microspheres (Invitrogen) added to the polyacrylamide

solution at a final concentration of 0.03% solids. Upon adding the polyacrylamide solution between two coverslips, the coverslip “sandwiches” were centrifuged in swing-buckets at $200 \times g$ for 10 min with the Rain-X coverslip at the bottom, and incubated in this configuration at room temperature for an additional 1 h to allow for polymerization. The centrifugation step forced all the microspheres into a single XY-plane at what ultimately became the surface of the hydrogel upon removal of the Rain-X coverslip.

hESC colonies were plated onto hydrogels as described in the following section. At timepoints for which traction force measurements were desired, images of the fluorescent microspheres (“stressed images”) were captured using a Nikon Eclipse TE200 U (Nikon) inverted microscope with a 10x objective, equipped with a motorized positioning stage (Prior Scientific HLD 117) and an ORCA Flash 4.0LT CMOS camera (Hamamatsu). hESCs were then lysed using 2% sodium dodecyl sulfate (Sigma) and images were captured of the fluorescent microspheres from the same regions of interest (“unstressed images”). For each region of interest, “stressed” and “unstressed” images were aligned using Fiji software plugin Linear Alignment with SIFT (Schindelin et al., 2012). Bead movements resulting from cell traction forces were determined using a Fiji software plugin for computing particle image velocimetry (PIV) measurements (Tseng et al., 2012), and these PIV measurements were converted to traction stresses using the Fiji software plugin FTTC (Tseng et al., 2012). MATLAB (MathWorks) was used to visualize the maps of traction stress magnitudes. For the traction stress maps shown, binary masks representing hESC colony areas were generated from brightfield images and used to remove traction stress noise from regions outside the colony area. A 10-pixel-wide border of zero values was added to all traction stress maps of patterned triangle colonies to provide clearer visualization of the corners. The perceptually uniform colormap “inferno” was applied to all traction stress plots (Biguri, 2020).

Maps of average traction stress magnitudes for geometrically-confined colonies were generated by using brightfield images of the colonies to align replicate traction stress maps for each geometry. The replicate traction stress maps were then cropped to a uniform size, and magnitude values at each voxel were averaged across all the maps. The number of colonies used to generate average traction stress maps can be found in the figure captions. MATLAB (MathWorks) was used to determine the 99th percentile traction stress value (in Pascals) for each individual traction stress map of geometrically-confined triangle hESC colonies with (shCDH1 KD) and without (control) shCDH1 knockdown.

The code generated to analyze and display traction force data is publicly available on GitHub (https://github.com/jmmuncie/TF_hESC).

Plating hESCs onto Hydrogels—Twenty-four hours prior to plating hESCs, knockout-DMEM (Gibco) was added to the hydrogels and incubated at 37° C in a humidified cell culture incubator with 5% CO₂. Prior to plating on hydrogels, T-mNeonGreen reporter cells cultured on γ -irradiated PMEFs were passaged into secondary cultures in feeder-free conditions on tissue culture plastic coated with rBM and fed with PMEF-conditioned KSR media supplemented with 10 ng/ml bFGF (PeproTech). hESC lines that were maintained in feeder-free conditions (H9, H2B-mCherry, and shCDH1) were passaged to hydrogels

directly. hESCs were released from rBM-coated plastic via 10 min incubation at 37° C with 0.05% trypsin-EDTA (Gibco) supplemented with 10 µM Y-27632 (Tocris), and counted using a hemocytometer.

Unconfined colonies of hESCs were generated on non-patterned hydrogels by placing custom 3D-printing plating guides (3 mm diameter; CAD drawings available upon request) onto the surface of the hydrogels and pipetting 20,000 cells through each opening of the plating guides. Guides were removed after incubation for 1 h to ensure cell attachment.

Patterned hESC colonies were generated by seeding 200,000 cells onto each of the patterned gels and very gently replacing the media after 3 h to remove non-attached cells. T-mNeonGreen reporter cells were plated in PMEF-conditioned KSR media, while the other cell lines were plated in 50% PMEF-conditioned KSR, 50% E8 media (Gibco). For shCDH1 experiments, IPTG (200 µM; Sigma) was added to the media one passage (72 h) prior to seeding on hydrogels to induce shCDH1 knockdown. All cell lines were plated in media supplemented with 10 ng/ml bFGF (PeproTech) and 10 µM Y-27632 (Tocris). The Y-27632 was diluted out of the media over the course of 72 h to prevent dissociation of hESCs from the hydrogels: 24 h after plating, media was replaced with media containing 5 µM Y-27632; 48 h after plating, media was replaced with media lacking Y-27632; 72 h after plating, experiments began.

BMP4 Differentiation—Differentiation was induced by removing maintenance media from hESC colonies on hydrogels and replacing it with Stemline II Hematopoietic Stem Cell Expansion Medium (Sigma) supplemented with 10 ng/ml bFGF (PeproTech) and 50 ng/ml BMP4 (PeproTech). hESC colonies were differentiated for the amount of time described for each experiment. For shCDH1 experiments, IPTG (200 µM; Sigma) was added to the differentiation media in the knockdown condition to maintain shCDH1 knockdown. For Src inhibition experiments, the Src-family kinase inhibitor (PP1; 10 µM; Sigma) or equal volume of vehicle (DMSO) was added to the standard differentiation media. For Wnt inhibition experiments, the Wnt processing and secretion inhibitor (IWP-2; 2 µM; MedChem Express) or equal volume of vehicle (DMSO) was added to the standard differentiation media.

Time-lapse Imaging—hESC colonies seeded on polyacrylamide gels in custom 3D printed holders were loaded into a custom-built stage mount as previously described (L. Przybyla et al., 2016a; CAD drawings for gel holders and stage mount available upon request), and differentiation was induced as described in the preceding section. The stage mount was sealed, enabling a low-pressure flow of mixed gas containing 5% CO₂, 95% air (Airgas) to maintain the pH of standard differentiation media, and the mount was placed onto a motorized positioning stage (Prior Scientific HLD 117) attached to a Nikon Eclipse TE200 U (Nikon) inverted epifluorescent microscope. The microscope stage, condenser, and objectives were encased in a Plexiglas box and a forced air temperature feedback control (In Vivo Scientific) was used to maintain the temperature of the entire setup at 37° C. Images were captured using a 10x objective at specified timepoints.

“Gastrulation-like” nodes were manually identified and counted in colonies of H2B-mCherry cells by utilizing both brightfield and fluorescent images. “Gastrulation-like” nodes were initially identifiable as regions of increased cell density in both brightfield and fluorescent channels. Subsequently, as cells ingressed and formed additional layers that caused fluorescent light scattering, nodes appeared as regions that seemingly lacked mCherry signal, but clearly contained densely-packed cells as revealed by the brightfield channel.

“Gastrulation-like” nodes were manually counted in colonies of T-mNeonGreen reporter cells by identifying regions with detectable nuclear T-mNeonGreen expression above background levels. Nearly twice as many “gastrulation-like” nodes were identified by 48 h of differentiation using the T-reporter because by not relying on visible morphological changes, smaller nodes were identified with much higher sensitivity based on T-mNeonGreen expression alone.

The size of “gastrulation-like” nodes were measured manually in both H2B-mCherry and T-mNeonGreen hESC colonies using the NIS-Elements (Nikon) software. Lines were drawn and measured across each node along the radial axis of the colony (i.e. along the line connecting the center of the colony to the edge of the colony nearest each node), the axis along which nodes were observed to elongate. Thus, the measurement of node size over time was designed to be akin to measuring the anterior elongation of the primitive streak in the embryo.

The “distance from edge” measurements for “gastrulation-like” nodes identified in T-mNeonGreen hESC colonies after 36 h of BMP4 stimulation were likewise measured along the radial axis of the colony.

Analysis of cell movements based on particle image velocimetry (PIV) was performed using the FIJI plugin “Iterative PIV (Cross-Correlation)” (Tseng et al., 2012) on brightfield images of hESC colonies at 6 h time intervals with subsequent interrogation windows of 128, 64, and 32 pixels.

Maps of normalized average intensity of T-mNeonGreen expression for triangle, Pac-Man, and triangle-in-Pac-Man patterned colonies were generated by using brightfield images to align the colonies from each replicate and crop the images to a uniform size. For time-lapse experiments, background signal was first removed by subtracting the image of mNeonGreen background expression at 20 h of BMP4 stimulation (prior to detectable T-mNeonGreen expression above background) from the image of T-mNeonGreen expression at the timepoint of interest. Detectable T-reporter expression typically arose between 24 h and 30 h of BMP4 stimulation. To account for this variation, the 30 h timepoint was conservatively selected for generating average T-reporter expression plots intended to illustrate the spatial localization of mesoderm induction. For the triangle-in-Pac-Man colonies on tissue culture plastic, the raw T-mNeonGreen images from colonies fixed at 36 h of BMP4 treatment were used. The intensity values at each pixel in the resulting images were then divided by the number of replicates for each experiment, and summed across all the replicates to generate average expression plots. These average intensity maps were then normalized to the maximum

intensity value within each map and visualized using MATLAB (MathWorks; display script available at https://github.com/jmmuncie/TF_hESC). The perceptually uniform colormap “viridis” was applied to the normalized average intensity maps (Biguri, 2020).

Immunofluorescence Staining and Imaging—hESC colonies on polyacrylamide gels were fixed slowly in cold conditions to prevent detachment of cells from the hydrogels. Prior to fixation, hESC colonies on gels were placed on ice and gently rocked for 10 min. Media was removed, ice-cold 4% paraformaldehyde (Sigma) was carefully added, and the samples were fixed at 4° C overnight. Prior to fixation, samples for β -catenin-Y654 staining were briefly washed with a hot “TNS” solution of 0.03% Triton-X 100 (Sigma), 0.4% NaCl (Fisher) at 90° C, and shook vigorously for 30 s to remove cytosolic β -catenin but leave junction β -catenin intact, as described previously (Röper et al., 2018). A larger volume of ice-cold TNS was then immediately added to rapidly cool each sample, after which all the TNS was removed and replaced with ice-cold 4% paraformaldehyde and samples were fixed at 4° C overnight.

After fixation, all samples were washed 3× 10 min with PBS and then simultaneously blocked and permeabilized with a 1 h incubation at room temperature in “IF Buffer” containing 0.1% bovine serum albumin (Fisher), 0.2% Triton-X 100 (Sigma), 0.05% Tween-20 (Sigma), 130 mM NaCl (Fisher), 13 mM Na₂HPO₄ (Fisher), 3.5 mM NaH₂PO₄ (Fisher), and 0.05% sodium azide (Sigma), supplemented with 10% goat serum (Sigma). Samples were then incubated overnight with primary antibodies diluted in IF Buffer plus 10% goat serum at 4° C with gentle rocking. The next day, samples were washed 3× 10 min with IF Buffer at room temperature and then incubated for 2 h with secondary antibodies diluted in IF Buffer plus 10% goat serum at room temperature with gentle shaking. Samples were then washed 3× 10 min with IF Buffer, 1× 5 min with 0.5 μ g/ml DAPI (Invitrogen) in PBS, and 2× 10 min with PBS. Samples were then removed from the custom gel holders, inverted onto #1 22 × 55 mm glass coverslips (VWF) and imaged. Epifluorescent images were captured using a Nikon Eclipse TE200 U (Nikon) inverted microscope with a 10x, 20x, or 60x objective and an ORCA Flash 4.0LT CMOS camera (Hamamatsu). Confocal images were captured using a Nikon Eclipse Ti inverted microscope (Nikon) equipped with a 60x objective, a CSU-X1 spinning disk confocal scanner (Yokogawa), and a Zyla sCMOS camera (Andor). Imaris software (Oxford Instruments) was used to perform z-stack reconstructions.

Primary antibodies used were: anti-T(brachyury) (RRID: AB_2200235, R&D Systems, 1:40), anti-E-cadherin (RRID: AB_2291471, CST, 1:200), anti-Slug (RRID: AB_2239535, CST, 1:400), anti-Fibronectin (RRID: AB_470662, Abcam, 1 μ g/ml), anti- β -catenin-Y654 (RRID: AB_10623284, Sigma, 1:50), anti- β -catenin (RRID: AB_11127855, CST, rabbit, 1:200), anti- β -catenin (ECM Biosciences, mouse, 1:250), anti-phospho-Src Family (RRID: AB_10013641, CST, 1:100), anti-POU5F1 (RRID: AB_2167703, Santa Cruz Biotechnology, 1:100). Secondary antibodies used were: Alexa Fluor 488 goat anti-mouse IgG (RRID: AB_2576208, Abcam, 1:1000), Alexa Fluor 568 goat anti-mouse IgG (Abcam, 1:1000), Alexa Fluor 488 goat anti-rabbit IgG (RRID: AB_2630356, Abcam, 1:1000), Alexa Fluor 568 goat anti-rabbit IgG (RRID: AB_2576207, Abcam, 1:1000), Alexa Fluor 488 donkey anti-goat IgG (RRID: AB_2687506, Abcam, 1:1000). Note: when anti-T(brachyury)

and Alexa Fluor 488 donkey anti-goat IgG antibodies were used, donkey serum was used in place of goat serum during all blocking and staining steps described above.

Images were analyzed in Fiji (Schindelin et al., 2012), unless otherwise noted.

Quantification of correlation between the T-mNeonGreen reporter expression and the T-antibody was performed by first pre-processing images by histogram matching all images from each channel to a randomly selected image from the same channel. After pre-processing, nuclei were identified and counted from images of DAPI staining using a trained classifier in the Pixel Classification pipeline of ilastik (Berg et al., 2019). Training was performed with 8 images. Next, the probability maps of the nuclei were processed with an ImageJ Jython script that used a Minimum filter (sigma = 5), Median filter (sigma = 10), and a Gaussian Blur filter (sigma = 5). Filtered images were then auto-thresholded using the Moments method, and the Watershed function was applied. Using the ROI manager, the resulting ROIs from the nuclei thresholds were used to calculate the mean intensity values in the T-reporter and the T-antibody histogram-matched images. The mean intensity values for all nuclei-ROIs for all images for either T-reporter or T-antibody, across three independent experiments, were plotted against each other using Python, with a regression line indicating the level of correlation of the values between both channels.

Quantification of cell density was performed by first pre-processing images by histogram matching DAPI stained images in ImageJ using a randomly selected image. After pre-processing, nuclei were identified from DAPI staining using a trained classifier in the Cell Density Counting pipeline on ilastik. Training was performed with two independent data sets, separate from an additional three independent experiments used for analysis. A Jython script was used for post-processing the probability images output from ilastik. Probability images were processed first using a Gaussian Filter (sigma = 2), auto-thresholded using the Moments method, and then a Watershed algorithm was applied to separate overlapping nuclei. Brightfield images were used to construct an outline of each colony, by first subtracting background using the Rolling Ball method with a radius of 50 pixels, then applying the Gamma function with a value 1.70, a Gaussian Filter (sigma = 5), and finally creating a mask with the auto-thresholding method Otsu. Nuclei ROIs within the Brightfield outline were then counted using the Analyze Particles function and the area and centroid of each nuclei particle were recorded per image, along with the centroid of the Brightfield outline. To normalize the location of colonies, the X and Y centroid of each nuclei particle per colony were subtracted by the corresponding X and Y centroid value of the colony, such that the centroid of each colony would be at the origin (0, 0). With the normalized centroid values of all colonies, a Python script was used to coalesce all data per shape (circle, square, and triangle) and a Kernel Density Estimate (KDE) plot was calculated per shape using the Matplotlib and Seaborn packages. To represent the margins of each colony, the minimum and maximum X and Y centroid values from all colonies per shape were isolated during data collection and used to create a shaded range of colony edges, with a dashed line indicating the average value. Representative images were created using the same KDE plot, and for these plots, the colony outline was created using a ConvexHull function from the SciPy package around all the centroid values.

Plot of relative mean fluorescence intensity for E-cadherin expression was generated by cropping all images to equivalent sizes and measuring the raw integrated density (RawIntDen, sum of pixel values). The RawIntDen values were normalized by dividing the RawIntDen value for each replicate within an experiment by the maximum RawIntDen value measured within that experiment. These normalized values were then plotted. Plot of % nuclei area T-positive was generated by first subtracting background from T and DAPI stained images using the Rolling Ball method with a radius of 50 pixels, then thresholding and converting images to binary, and finally taking the ratio of the threshold area of the T staining relative to the threshold area of DAPI staining.

Quantification of β -catenin release from cell junctions was performed by measuring the fluorescence intensity profiles along lines of 60 pixels centered at cell junctions, for five cell junctions in each image analyzed. Measurements from all profiles from each condition were then normalized to the maximum value between compared conditions and plotted as mean \pm 95% CI for each condition.

Maps of normalized average intensity of β -catenin Y654 expression for triangle and Pac-Man patterned colonies were generated by using brightfield images to align the colonies from each replicate and crop the images to a uniform size. Images were then converted to “.txt” format and manipulated using MATLAB (MathWorks). Each replicate pair of images (triangle corner vs. middle and Pac-Man concave vs. convex) were normalized to the maximum intensity value of the pair. The intensity values at each pixel in the resulting images were then divided by the number of replicates for each experiment, and summed across all the replicates to generate average expression plots. These average intensity maps were then normalized to the maximum intensity value within each pair of maps (triangle corner average vs. middle average and Pac-Man concave average vs. convex average) and visualized (display script at https://github.com/jmmuncie/TF_hESC) using the perceptually uniform colormap “viridis” (Biguri, 2020).

Quantification of junctional pSFK expression was performed by using β -catenin to create masks of cell junctions within imaged regions and using these to mask junctional pSFK expression from total pSFK expression. Masks were created by subtracting background from images of β -catenin using the Rolling Ball method with a radius of 50 pixels, thresholding the background-subtracted images with the Otsu method, and dividing the resultant binary images by 255 such that pixel values were either zero or one. The Image Calculator function (FIJI) was used to multiply the β -catenin mask by the pSFK image for each region to mask junctional pSFK. The resultant junctional expression was measured (RawIntDen), normalized to the area of the β -catenin mask (junctional area), and these values were plotted.

Quantitative PCR (qPCR)—Total RNA was isolated from either full colonies of hESCs or FACS-sorted populations of T-mNeonGreen reporter cells as indicated in the main text and figure captions using TRIzol (Invitrogen) according to the manufacturer’s protocol. cDNA was synthesized from RNA using M-MLV Reverse Transcriptase (BioChain) and Random Hexamers (Applied Biosystems) as primers. qPCR was performed in triplicates from 10 ng of RNA per reaction using PerfeCTa SYBR Green FastMix (Quantabio) on a Mastercycler RealPlex² detection system (Eppendorf). All reactions for qPCR were

performed using the following conditions: 95 °C for 30 s followed by 40 cycles of a three-step reaction of denaturation at 95 °C for 10 s, annealing at 65 °C for 10 s, and further annealing at 68 °C for 20 s to reduce the likelihood of non-specific products, with reads taken at the end of each 68 °C step. At the end of each reaction, melting curves were generated to validate the quality of amplified products using the following conditions: 95 °C for 15 s, 60 °C for 15 s, ramp to 95 °C in 10 min. The mean Ct values from triplicates were used to calculate the Ct values relative to GAPDH expression. The means of the Ct values from independent experiments were used to calculate mean fold change of expression using the 2^{-Ct} method. For each gene evaluated, the 95% CI of the Ct values was calculated and used to generate positive and negative error values in the 2^{-Ct} fold change space. Plots of qPCR data display line and bars representing the mean fold change \pm 95% CI and individual points representing the fold change value for each experimental replicate relative to the mean. All primers used in this study are listed in Table S1.

Eyebrow Knife Experiment—Eyebrow knives were fabricated by first heating 5.75” borosilicate glass Pasteur pipets (Fisher) over a Bunsen burner and pulling to generate a narrower tip. Paraffin wax (Sigma) was used to attach a plucked human eyebrow hair to the narrow tip of the pipet. (Note: Variations in the thickness and density of eyebrow hair will affect the ability to effectively manipulate hESC colonies, therefore, different eyebrow hairs from multiple individuals should be tested when adopting this method). “Stressed” microsphere images were captured for triangle patterned colonies of T-mNeonGreen reporter cells, as described in the “Traction Force Microscopy” section, prior to being cut with the eyebrow knife. Next, a Nikon SMZ800 (Nikon) dissecting microscope was used to make precise cuts with an eyebrow knife through the corners of triangle patterned colonies and additional “stressed” microsphere images were captured following the eyebrow knife cuts. The colonies were differentiated with BMP4 and time-lapse imaging was conducted to monitor T-mNeonGreen expression, as described in the “Time-lapse Imaging” section. After 48 h of differentiation, cells were lysed with 2% SDS (Sigma) and “unstressed” microsphere images were captured. Finally, the microsphere images were used to generate plots of traction stress magnitude for the colonies before and after cutting with the eyebrow knife and compared to the spatiotemporal expression of T-mNeonGreen captured during the time-lapse imaging.

The plot of time to T-mNeonGreen expression was generated by analyzing the time-lapse imaging data at each corner of the triangle patterned colonies successfully cut with the eyebrow knife. Each corner was categorized as “cut” or “intact” and the timepoint at which nuclear expression of T-mNeonGreen was detectable above background for cells within each corner was recorded and plotted.

Mechanical Stretching via Microfluidic Device—The microfluidic cell stretching device comprised a PDMS structural layer, a PDMS inlet block and a glass coverslip. The PDMS structural layer, which contained a microfluidic network for applying pressure to simultaneously activate 64 pressurization compartments to induce PDMS membrane deformation, was fabricated using soft lithography. Briefly, the PDMS pre-polymer was spin-coated onto a silicon mold generated using photolithography and deep reactive ion

etching (DRIE). The PDMS layer was thermally cured at 110 °C for at least 24 h before being peeled off the silicon mold. An inlet for fluid connections was then punched into the PDMS structural layer using a 1 mm biopsy punch (Fisher). Both the coverslip and the PDMS structural layer were briefly cleaned with 100% ethanol (Fisher) and blown dry under nitrogen gas before being treated with air plasma (Plasma Prep II; SPI Supplies) and bonded together. In parallel, another PDMS block was prepared, and an inlet for fluid connection was punched into the PDMS block with a 0.5 mm biopsy punch. After treating both with air plasma, the PDMS block and the PDMS structural layer were bonded together with their fluid inlets aligned manually. The microfluidic cell stretching device was baked at 110 °C for at least another 24 h to ensure robust bonding between layers. Deionized water was injected into the microfluidic cell stretching device before applying pressure through a microfluidic pressure pump (AF1, Elveflow). Elveflow Smart Interface software (<https://www.elveflow.com/>) was used for programming the pressure pump for continuous cell stretching with a square-wave pattern (pulse width of 2 h, period of 4 h and 50% duty cycle), which was applied coincident with the start and maintained throughout the 48 h BMP4 differentiation.

Microcontact printing was performed to print circular adhesive patterns with a diameter of 400 µm onto the deformable PDMS membrane on top of the pressurization compartments (with a diameter of 200 µm) in the custom-designed microfluidic cell stretching device. To this end, a custom desktop aligner designed for fabrication of multilayer microfluidic devices was used (Li et al., 2015). Briefly, a vitronectin-coated (20 µg/ml; Trevigen) PDMS stamp and the microfluidic cell stretching device were mounted onto the top and bottom layer holders of the aligner, respectively. Under a digital microscope, the X/Y/θ stage holding the bottom layer holder was carefully adjusted to align the PDMS stamp and the microfluidic cell stretching device. The PDMS stamp was then gently pressed to achieve conformal contact with the microfluidic cell stretching device to transfer vitronectin from the stamp to the PDMS membrane on top of the pressurization compartments.

The plots of average T-mNeonGreen expression in control and stretched colonies after 48 h were generated by dividing the intensity values at each pixel in the T-mNeonGreen images by the number of replicates for each condition, and then summing all the replicate images. These average intensity maps were then normalized to the maximum intensity value within each map and visualized using MATLAB (MathWorks; display script available at https://github.com/jmmuncie/TF_hESC). The perceptually uniform colormap “viridis” was applied to the normalized average intensity maps (Biguri, 2020).

In Situ Hybridization via Hybridization Chain Reaction (ISH-HCR)—Third-generation ISH-HCR was performed as described previously (Choi et al., 2018). Samples were fixed slowly in cold conditions to prevent detachment of hESCs from the hydrogels. Prior to fixation, hESC colonies on gels were placed on ice and gently rocked for 10 min. Media was removed, ice-cold 4% paraformaldehyde (Sigma) was carefully added, and the samples were fixed at 4° C overnight. The next day, samples were washed 3× 10 min with diethyl pyrocarbonate (DEPC; Sigma) treated PBS with 0.1% Tween-20 (Sigma) to permeabilize, and then washed 1× 5 min with 5x SSC buffer with 0.1% Tween-20. Samples were incubated for 1 h at 37° C in a humidified chamber in hybridization buffer consisting

of 30% de-ionized formamide (Sigma), 5x SSC, 9 mM citric acid, pH 6.0 (Sigma), 0.1% Tween-20, 50 µg/ml heparin (Sigma), 1x Denhardt's solution (Sigma), 10% dextran sulfate, avg $M_w > 500,000$ (Sigma), and DEPC-treated ultrapure water. Samples were then hybridized overnight via incubation at 37° C in a humidified chamber with hybridization buffer plus 20 nM split initiator hybridization probes designed to target WNT3A (Table S2) and 10 mM ribonucleoside vanadyl complexes (Sigma). The next day, samples were washed 5× 10 min at 37° C with no agitation using a buffer consisting of 30% formamide, 5x SSC, and 9 M citric acid, pH 6.0. Samples were further washed 3× 10 min at room temperature with gentle shaking using a buffer of 5x SSC, 0.1% Tween-20, and 50 µg/ml heparin. Samples were incubated for 30 min at room temperature in amplification buffer consisting of 5x SSC, 0.1% Tween-20, and 10% dextran sulfate, avg $M_w > 500,000$. Samples were then incubated overnight at room temperature in amplification buffer plus 60 nM HCR3 amplification probes conjugated with Alexa Fluor 647 (Choi et al., 2018). The next day, samples were washed 5× 10 min at room temperature with gentle shaking in 5x SSC with 0.1% Tween-20. The third wash also contained 0.5 µg/ml DAPI (Invitrogen). Finally, samples were inverted onto #1 22 × 55 mm glass coverslips (VWF) and imaged using a Nikon Eclipse Ti inverted microscope (Nikon) equipped with a 60x objective, a CSU-X1 spinning disk confocal scanner (Yokogawa), and a Zyla sCMOS camera (Andor). Split initiator hybridization probe sequences targeting WNT3A mRNA transcripts are listed in Table S2.

Quantification of ISH-HCR speckles was performed by first subtracting background from WNT3A-ISH images using the Rolling Ball method with a radius of 20 pixels and thresholding the resulting images. The Analyze Particles function (FIJI) was then used to count speckles within each image, with min-max size parameters set to 5-Infinity pixels and min-max circularity parameters set to 0.3–1.0. In order to determine an approximation of speckles per cell within each analyzed image, nuclei were identified and counted from images of DAPI staining using the Primary Object Identifier in CellProfiler (McQuin et al., 2018). Speckle counts for each imaged region were then divided by the number of nuclei identified and these values were plotted.

QUANTIFICATION AND STATISTICAL ANALYSIS

Tests of significance for comparisons between two experimental groups were performed using the two-tailed unpaired Student's t-test in Prism 6 software (GraphPad), except for the data presented in Figure panels 6F and 7F, for which one-tailed unpaired Student's t-tests were used because previous results suggested the expected direction of change in gene expression levels. Tests of significance for comparisons between more than two experimental groups were performed using a one-way Analysis of Variance (ANOVA) test in Prism 6 software (GraphPad). Parametric tests were used to provide greater statistical power and to avoid assumptions of symmetric distributions and/or equal variance between groups required by nonparametric tests. Differences were determined to be statistically significant at $p < 0.05$, and statistical significance was denoted by asterisks in the figure panels, with * = $p < 0.05$, ** = $p < 0.01$, *** = $p < 0.001$, **** = $p < 0.0001$. Differences that were determined to not be statistically significant were either denoted "n.s." or the p-value was noted above the data. For immunofluorescent image data, the figure panels illustrate representative

results from at least $n = 3$ independent experiments where a minimum of three replicate hESC colonies were imaged for each condition in each experiment. For qPCR data $n =$ the number of independent experiments, with hESCs pooled from at least three different hydrogels for each condition in each experiment. All other definitions of n can be found in the figure captions. Where plotted, bars and lines represent mean \pm 95% confidence interval (CI) of the data. Statistical parameters plotted in each figure are also described in the figure captions.

Supplementary Material

Refer to Web version on PubMed Central for supplementary material.

Acknowledgements

We thank Lisandro Maya-Ramos and Takashi Mikawa for assistance with chicken embryo manipulation. We also thank Roberto Falc3n-Banchs and Lydia L. Sohn, as well as Benjamin Demaree and Adam R. Abate, for assistance with soft lithography techniques. The authors would like to acknowledge funding from CIRM grant RB5-07409, NIH/NCI U01 grant CA202241, and National Science Foundation (CMMI 1917304; J. Fu). Additionally, J.M.M. is thankful for support from the UCSF Discovery Fellowship.

References

- Beccari L, Moris N, Girgin M, Turner DA, Baillie-Johnson P, Cossy AC, Lutolf MP, Duboule D, Arias AM, 2018 Multi-axial self-organization properties of mouse embryonic stem cells into gastruloids. *Nature* 562(7726), 272–276. [PubMed: 30283134]
- Berg S, Kutra D, Kroeger T, Straehle CN, Kausler BX, Haubold C, Schiegg M, Ales J, Beier T, Rudy M, Eren K, Cervantes JI, Xu B, Beuttenmueller F, Wolny A, Zhang C, Koethe U, Hamprecht FA, Kreshuk A, 2019 ilastik: interactive machine learning for (bio)image analysis. *Nat. Methods*. 1–7. [PubMed: 30573832]
- Bertocchini F, Stern CD, 2002 The hypoblast of the chick embryo positions the primitive streak by antagonizing nodal signaling. *Dev. Cell*. 3(5), 735–744. [PubMed: 12431379]
- Bienz M, 2005 β -catenin: A pivot between cell adhesion and Wnt signalling. *Curr. Biol*. 15(2), R64–R67. [PubMed: 15668160]
- Biguri A, 2020 Perceptually uniform colormaps. (<https://www.mathworks.com/matlabcentral/fileexchange/51986-perceptually-uniform-colormaps>), MATLAB Central File Exchange Retrieved April 24, 2020.
- Blin G, Wisniewski D, Picart C, They M, Puceat M, Lowell S, 2018 Geometrical confinement controls the asymmetric patterning of brachyury in cultures of pluripotent cells. *Dev*. 145(18).
- Brunet T, Bouclet A, Ahmadi P, Mitrossilis D, Driquez B, Brunet AC, Henry L, Serman F, B3alle G, M3nager C, Dumas-Bouchiat F, Givord D, Yanicostas C, Le-Roy D, Dempsey NM, Plessis A, Farge E, 2013 Evolutionary conservation of early mesoderm specification by mechanotransduction in Bilateria. *Nat. Commun*. 4(1), 1–15.
- Chapman SC, Collignon J, Schoenwolf GC, Lumsden A, 2001 Improved method for chick whole-embryo culture using a filter paper carrier. *Dev. Dyn*. 220(3), 284–289. [PubMed: 11241836]
- Cheng S, Fockler C, Barnes WM, Higuchi R, 1994 Effective amplification of long targets from cloned inserts and human genomic DNA. *Proc. Natl. Acad. Sci*. 91(12), 5695–5699. [PubMed: 8202550]
- Chhabra S, Liu L, Goh R, Kong X, Warmflash A, 2019 Dissecting the dynamics of signaling events in the BMP, WNT, and NODAL cascade during self-organized fate patterning in human gastruloids. *PLoS Biol*. 17(10), e3000498. [PubMed: 31613879]
- Choi HMT, Schwarzkopf M, Fornace ME, Acharya A, Artavanis G, Stegmaier J, Cunha A, Pierce NA, 2018 Third-generation in situ hybridization chain reaction: Multiplexed, quantitative, sensitive, versatile, robust. *Development* 145(12), dev165753. [PubMed: 29945988]

- Chu VT, Weber T, Wefers B, Wurst W, Sander S, Rajewsky K, Kühn R, 2015 Increasing the efficiency of homology-directed repair for CRISPR-Cas9-induced precise gene editing in mammalian cells. *Nat. Biotechnol.* 33(5), 543–548. [PubMed: 25803306]
- Clevers H, 2006 Wnt/ β -catenin signaling in development and disease. *Cell* 127(3), 469–480. [PubMed: 17081971]
- Cong L, Ran FA, Cox D, Lin S, Barretto R, Habib N, Hsu PD, Wu X, Jiang W, Marraffini LA and Zhang F, 2013 Multiplex genome engineering using CRISPR/Cas systems. *Science* 339(6121), 819–823. [PubMed: 23287718]
- Davidson LA, Dzamba BD, Keller R, Desimone DW, 2008 Live imaging of cell protrusive activity, and extracellular matrix assembly and remodeling during morphogenesis in the frog, *Xenopus laevis*. *Dev. Dyn.* 237(10), 2684–2692. [PubMed: 18629871]
- Eliazer S, Muncie JM, Christensen J, Sun X, D'Urso RS, Weaver VM, Brack AS, 2019 Wnt4 from the niche controls the mechano-properties and quiescent state of muscle stem cells. *Cell Stem Cell* 25(5), 654–665. [PubMed: 31495781]
- Etoc F, Metzger J, Ruzo A, Kirst C, Yoney A, Ozair MZ, Brivanlou AH, Siggia ED, 2016 A balance between secreted inhibitors and edge sensing controls gastruloid self-organization. *Dev. Cell* 39(3), 302–315. [PubMed: 27746044]
- Gayraud C, Bernaudin C, Déjardin T, Seiler C, Borghi N, 2018 Src- and confinement-dependent FAK activation causes E-cadherin relaxation and β -catenin activity. *J. Cell Biol.* 217(3), 1063–1077. [PubMed: 29311227]
- Gomez EW, Chen QK, Gjorevski N, Nelson CM, 2010 Tissue geometry patterns epithelial-mesenchymal transition via intercellular mechanotransduction. *J. Cell. Biochem.* 110(1), 44–51. [PubMed: 20336666]
- Gottardi CJ, Gumbiner BM, 2004 Distinct molecular forms of β -catenin are targeted to adhesive or transcriptional complexes. *J. Cell Biol.* 167(2), 339–349. [PubMed: 15492040]
- Hamada H, 2015 Role of physical forces in embryonic development In: *Semin. Cell Dev. Biol.*, Sampath K, Hiiragi T, Hadjantonakis K, ed. (Exeter, UK: Academic Press, Elsevier), 88–91.
- Hamburger V, Hamilton HL, 1992 A series of normal stages in the development of the chick embryo. *Dev. Dyn.* 195(4), 231–272. [PubMed: 1304821]
- Harrison SE, Sozen B, Christodoulou N, Kyprianou C, Zernicka-Goetz M, 2017 Assembly of embryonic and extraembryonic stem cells to mimic embryogenesis in vitro. *Science* 356(6334).
- Howard S, Deroo T, Fujita Y, Itasaki N, 2011 A positive role of cadherin in wnt/ β -catenin signalling during epithelial-mesenchymal transition. *PLoS One* 6(8).
- Howden SE, Wardan H, Voullaire L, McLenachan S, Williamson R, Ioannou P, Vadolas J, 2006 Chromatin-binding regions of EBNA1 protein facilitate the enhanced transfection of Epstein-Barr virus-based vectors. *Hum. Gene Ther.* 17(8), 833–844. [PubMed: 16942443]
- Keller R, 2005 Cell migration during gastrulation. *Curr. Opin. Cell Biol.* 17(5), 533–541. [PubMed: 16099638]
- Kemp C, Willems E, Abdo S, Lambiv L, Leyns L, 2005 Expression of all Wnt genes and their secreted antagonists during mouse blastocyst and postimplantation development. *Dev. Dyn.* 233(3), 1064–1075. [PubMed: 15880404]
- Kilian KA, Bugarija B, Lahn BT, Mrksich M, 2010 Geometric cues for directing the differentiation of mesenchymal stem cells. *Proc. Natl. Acad. Sci.* 107(11), 4872–4877. [PubMed: 20194780]
- Ko CS, Martin AC, 2020 The cellular and molecular mechanisms that establish the mechanics of *Drosophila* gastrulation In: *Current Topics in Developmental Biology*, Solnica-Krezel L, ed. (Cambridge, MA, USA: Academic Press, Elsevier), 141–166.
- Koch F, Scholze M, Wittler L, Schifferl D, Sudheer S, Grote P, Timmermann B, Macura K, Herrmann BG, 2017 Antagonistic activities of Sox2 and brachyury control the fate choice of neuro-mesodermal progenitors. *Dev. Cell* 42(5), 514–526. [PubMed: 28826820]
- Kyprianou C, Christodoulou N, Hamilton RS, Nahaboo W, Boomgaard DS, Amadei G, Migeotte I, Zernicka-Goetz M, 2020 Basement membrane remodelling regulates mouse embryogenesis. *Nature* 1–6.

- Lakins JN, Chin AR, Weaver VM, 2012 Exploring the link between human embryonic stem cell organization and fate using tension-calibrated extracellular matrix functionalized polyacrylamide gels In: Progenitor Cells, Mace KA, Braun KM, ed. (Totowa, NJ, USA: Humana Press), 317–350.
- Lee HC, Lu HC, Turmaine M, Oliveira NMM, Yang Y, De Almeida I, Stern CD, 2020 Molecular anatomy of the pre-primitive-streak chick embryo. *Open Biol.* 10(2), 190299. [PubMed: 32102607]
- Lee J, Abdeen AA, Wycislo KL, Fan TM, Kilian KA, 2016 Interfacial geometry dictates cancer cell tumorigenicity. *Nat. Mater.* 15(8), 856–862. [PubMed: 27043781]
- Li X, Yu ZTF, Geraldo D, Weng S, Alve N, Dun W, Kini A, Patel K, Shu R, Zhang F, Li G, Jin Q, Fu J, 2015 Desktop aligner for fabrication of multilayer microfluidic devices. *Rev. Sci. Instrum.* 86(7), 075008. [PubMed: 26233409]
- Lilien J, Balsamo J, 2005 The regulation of cadherin-mediated adhesion by tyrosine phosphorylation/dephosphorylation of β -catenin. *Curr. Opin. Cell Biol.* 17(5), 459–465. [PubMed: 16099633]
- Lindsley RC, Gill JG, Kyba M, Murphy TL, Murphy KM, 2006 Canonical Wnt signaling is required for development of embryonic stem cell-derived mesoderm. *Dev.* 133(19), 3787–3796.
- Manfrin A, Tabata Y, Paquet ER, Vuaridel AR, Rivest FR, Naef F, Lutolf MP, 2019 Engineered signaling centers for the spatially controlled patterning of human pluripotent stem cells. *Nat. Methods* 16(7), 640. [PubMed: 31249412]
- Martyn I, Brivanlou AH, Siggia ED, 2019 A wave of WNT signaling balanced by secreted inhibitors controls primitive streak formation in micropattern colonies of human embryonic stem cells. *Dev.* 146(6), dev172791.
- McMillen P, Holley SA, 2015 The tissue mechanics of vertebrate body elongation and segmentation. *Curr. Opin. Genet. Dev.* 32, 106–111. [PubMed: 25796079]
- McQuin C, Goodman A, Chernyshev V, Kamensky L, Cimini BA, Karhohs KW, Doan M, Ding L, Rafelski SM, Thirstrup D, Wiegraebe W, Singh S, Becker T, Caicedo JC, Carpenter AE, 2018 CellProfiler 3.0: Next-generation image processing for biology. *PLoS Biol.* 16(7), e2005970. [PubMed: 29969450]
- Mikawa T, Poh AM, Kelly KA, Ishii Y, Reese DE, 2004 Induction and patterning of the primitive streak, an organizing center of gastrulation in the amniote. *Dev. Dyn.* 229(3), 422–432. [PubMed: 14991697]
- Muncie JM, Falcón-Banchs R, Lakins JN, Sohn LL, Weaver VM, 2019 Patterning the Geometry of Human Embryonic Stem Cell Colonies on Compliant Substrates to Control Tissue-Level Mechanics. *J. Vis. Exp.* 10.3791/60334
- Nelson CM, VanDuijn MM, Inman JL, Fletcher DA, Bissell MJ, 2006 Tissue geometry determines sites of mammary branching morphogenesis in organotypic cultures. *Science* 314(5797), 298–300. [PubMed: 17038622]
- Paré AC, Zallen JA, 2020 Cellular, molecular, and biophysical control of epithelial cell intercalation In: *Current Topics in Developmental Biology*, Solnica-Krezel L, ed. (Cambridge, MA, USA: Academic Press, Elsevier), 167–194.
- Petersen CP, Reddien PW, 2009 Wnt signaling and the polarity of the primary body axis. *Cell* 139(6), 1056–1068. [PubMed: 20005801]
- Przybyla L, Lakins JN, Sunyer R, Trepatt X, Weaver VM, 2016a Monitoring developmental force distributions in reconstituted embryonic epithelia. *Methods* 94, 101–113. [PubMed: 26342256]
- Przybyla L, Lakins JN, Weaver VM, 2016b Tissue Mechanics Orchestrate Wnt-Dependent Human Embryonic Stem Cell Differentiation. *Cell Stem Cell* 19(4), 462–475. [PubMed: 27452175]
- Ramasubramanian A, Chu-Lagraff QB, Buma T, Chico KT, Carnes ME, Burnett KR, Bradner SA, Gordon SS, 2013 On the role of intrinsic and extrinsic forces in early cardiac S-looping. *Dev. Dyn.* 242(7), 801–816. [PubMed: 23553909]
- Röper JC, Mitrossilis D, Stirnemann G, Waharte F, Brito I, Fernandez-Sanchez ME, Baaden M, Salamero J, Farge E, 2018 The major β -catenin/E-cadherin junctional binding site is a primary molecular mechano-transducer of differentiation in vivo. *Elife* 7, e33381. [PubMed: 30024850]
- Saadaoui M, Rocancourt D, Roussel J, Corson F, Gros J, 2020. A tensile ring drives tissue flows to shape the gastrulating amniote embryo. *Science* 367(6476), 453–458. [PubMed: 31974255]

- Sagy N, Slovin S, Allalouf M, Pour M, Savyon G, Boxman J, Nachman I, 2019 Prediction and control of symmetry breaking in embryoid bodies by environment and signal integration. *Dev.* 146(20), dev181917.
- San Filippo J, Sung P, Klein H, 2008 Mechanism of eukaryotic homologous recombination. *Annu. Rev. Biochem.* 77, 229–257. [PubMed: 18275380]
- Schindelin J, Arganda-Carreras I, Frise E, Kaynig V, Longair M, Pietzsch T, Preibisch S, Rueden C, Saalfeld S, Schmid B, Tinevez JY, White DJ, Hartenstein V, Eliceiri K, Tomancak P, Cardona A, 2012 Fiji: An open-source platform for biological-image analysis. *Nat. Methods* 9(7), 676–682. [PubMed: 22743772]
- Shahbazi MN, Jedrusik A, Vuoristo S, Recher G, Hupalowska A, Bolton V, Fogarty NME, Campbell A, Devito LG, Ilic D, Khalaf Y, Niakan KK, Fishel S, Zernicka-Goetz M, 2016 Self-organization of the human embryo in the absence of maternal tissues. *Nat. Cell Biol.* 18(6), 700–708. [PubMed: 27144686]
- Shahbazi MN, Siggia ED, Zernicka-Goetz M, 2019 Self-organization of stem cells into embryos: A window on early mammalian development. *Science* 364(6444), 948–951. [PubMed: 31171690]
- Shahbazi MN, Zernicka-Goetz M, 2018 Deconstructing and reconstructing the mouse and human early embryo. *Nat. Cell Biol.* 20(8), 878–887. [PubMed: 30038253]
- Shao Y, Taniguchi K, Townshend RF, Miki T, Gumucio DL, Fu J, 2017 A pluripotent stem cell-based model for post-implantation human amniotic sac development. *Nat. Commun.* 8(1), 1–15. [PubMed: 28232747]
- Simunovic M, Brivanlou AH, 2017 Embryoids, organoids and gastruloids: new approaches to understanding embryogenesis. *Development* 144(6), 976–985. [PubMed: 28292844]
- Simunovic M, Metzger JJ, Etoc F, Yoney A, Ruzo A, Martyn I, Croft G, You DS, Brivanlou AH, Siggia ED, 2019 A 3D model of a human epiblast reveals BMP4-driven symmetry breaking. *Nat. Cell Biol.* 21(7), 900–910. [PubMed: 31263269]
- Sive HL, Grainger RM, Harland RM, 2000 Early development of *Xenopus laevis*: A laboratory manual (Cold Spring Harbor, NY, USA: CSHL Press).
- Smith Q, Rochman N, Carmo AM, Vig D, Chan XY, Sun S, Gerecht S, 2018 Cytoskeletal tension regulates mesodermal spatial organization and subsequent vascular fate. *Proc. Natl. Acad. Sci.* 115(32), 8167–8172. [PubMed: 30038020]
- Sozen B, Amadei G, Cox A, Wang R, Na E, Czukiewska S, Chappell L, Voet T, Michel G, Jing N, Glover DM, Zernicka-Goetz M, 2018 Self-assembly of embryonic and two extra-embryonic stem cell types into gastrulating embryo-like structures. *Nat. Cell Biol.* 20(8), 979–989. [PubMed: 30038254]
- Spratt NT, Haas H, 1960 Integrative mechanisms in development of the early chick blastoderm. I. Regulative potentiality of separated parts. *J. Exp. Zool.* 145(2), 97–137.
- Taber LA, 2014 Morphomechanics: Transforming tubes into organs. *Curr. Opin. Genet. Dev.* 27, 7–13. [PubMed: 24791687]
- Tewary M, Dziedzicka D, Ostblom J, Prochazka L, Shakiba N, Heydari T, Aguilar-Hidalgo D, Woodford C, Piccinini E, Becerra-Alonso D, Vickers A, Louis B, Rahman N, Danovi D, Geens M, Watt FM, Zandstra PW, 2019 High-throughput micropatterning platform reveals Nodal-dependent bisection of peri-gastrulation-associated versus preneurulation-associated fate patterning. *PLoS Biol.* 17(10).
- Tewary M, Ostblom J, Prochazka L, Zulueta-Coarasa T, Shakiba N, Fernandez-Gonzalez R, Zandstra PW, 2017 A stepwise model of reaction-diffusion and positional information governs self-organized human peri-gastrulation-like patterning. *Development* 144(23), 4298–4312. [PubMed: 28870989]
- Tseng Q, Duchemin-Pelletier E, Deshiere A, Bolland M, Guilloud H, Filhol O, The y M, 2012 Spatial organization of the extracellular matrix regulates cell-cell junction positioning. *Proc. Natl. Acad. Sci.* 109(5), 1506–1511. [PubMed: 22307605]
- Turlier H, Maître JL, 2015 Mechanics of tissue compaction In: *Semin. Cell Dev. Biol.* Sampath K, Hiiragi T, Hadjantonakis K, ed. (Exeter, UK: Academic Press, Elsevier), 110–117.

- Urlinger S, Baron U, Thellmann M, Hasan MT, Bujard H, Hillen W, 2000 Exploring the sequence space for tetracycline-dependent transcriptional activators: Novel mutations yield expanded range and sensitivity. *Proc. Natl. Acad. Sci.* 97(14), 7963–7968. [PubMed: 10859354]
- van Amerongen R, Nusse R, 2009 Towards an integrated view of Wnt signaling in development. *Development* 136(19), 3205–3214. [PubMed: 19736321]
- van den Brink SC, Alemany A, van Batenburg V, Moris N, Blotenburg M, Vivié J, Baillie-Johnson P, Nichols J, Sonnen KF, Martinez Arias A, van Oudenaarden A, 2020 Single-cell and spatial transcriptomics reveal somitogenesis in gastruloids. *Nature* 1–5.
- Van Den Brink SC, Baillie-Johnson P, Balayo T, Hadjantonakis AK, Nowotschin S, Turner DA, Arias AM, 2014 Symmetry breaking, germ layer specification and axial organisation in aggregates of mouse embryonic stem cells. *Dev.* 141(22), 4231–4242.
- Vijayraghavan DS, Davidson LA, 2017 Mechanics of neurulation: From classical to current perspectives on the physical mechanics that shape, fold, and form the neural tube. *Birth defects research* 109(2), 153–168. [PubMed: 27620928]
- Voiculescu O, Bodenstern L, Jun IL, Stern CD, 2014 Local cell interactions and self-amplifying individual cell ingression drive amniote gastrulation. *Elife* 3, e01817. [PubMed: 24850665]
- Warmflash A, Sorre B, Etoc F, Siggia ED, Brivanlou AH, 2014 A method to recapitulate early embryonic spatial patterning in human embryonic stem cells. *Nat. Methods* 11(8), 847–854. [PubMed: 24973948]
- Williams ML, Solnica-Krezel L, 2017 Regulation of gastrulation movements by emergent cell and tissue interactions. *Curr. Opin. Cell Biol.* 48, 33–39. [PubMed: 28586710]
- Xue X, Sun Y, Resto-Irizarry AM, Yuan Y, Aw Yong KM, Zheng Y, Weng S, Shao Y, Chai Y, Studer L, Fu J, 2018 Mechanics-guided embryonic patterning of neuroectoderm tissue from human pluripotent stem cells. *Nat. Mater.* 17(7), 633–641. [PubMed: 29784997]
- Zhang Z, Zwick S, Loew E, Grimley JS, Ramanathan S, 2019 Mouse embryo geometry drives formation of robust signaling gradients through receptor localization. *Nat. Commun.* 10(1), 1–14. [PubMed: 30602773]
- Zheng Y, Xue X, Shao Y, Wang S, Esfahani SN, Li Z, Muncie JM, Lakins JN, Weaver VM, Gumucio DL, Fu J, 2019 Controlled modelling of human epiblast and amnion development using stem cells. *Nature* 573(7774), 421–425. [PubMed: 31511693]

Highlights

- Substrates that recapitulate embryo elasticity promote hESC self-organization
- “Gastrulation-like” morphogenesis occurs in regions of high cell-adhesion tension
- Tissue geometry dictates the localization of high cell-adhesion tension
- Tension releases junctional β -catenin and drives Wnt signaling to specify mesoderm

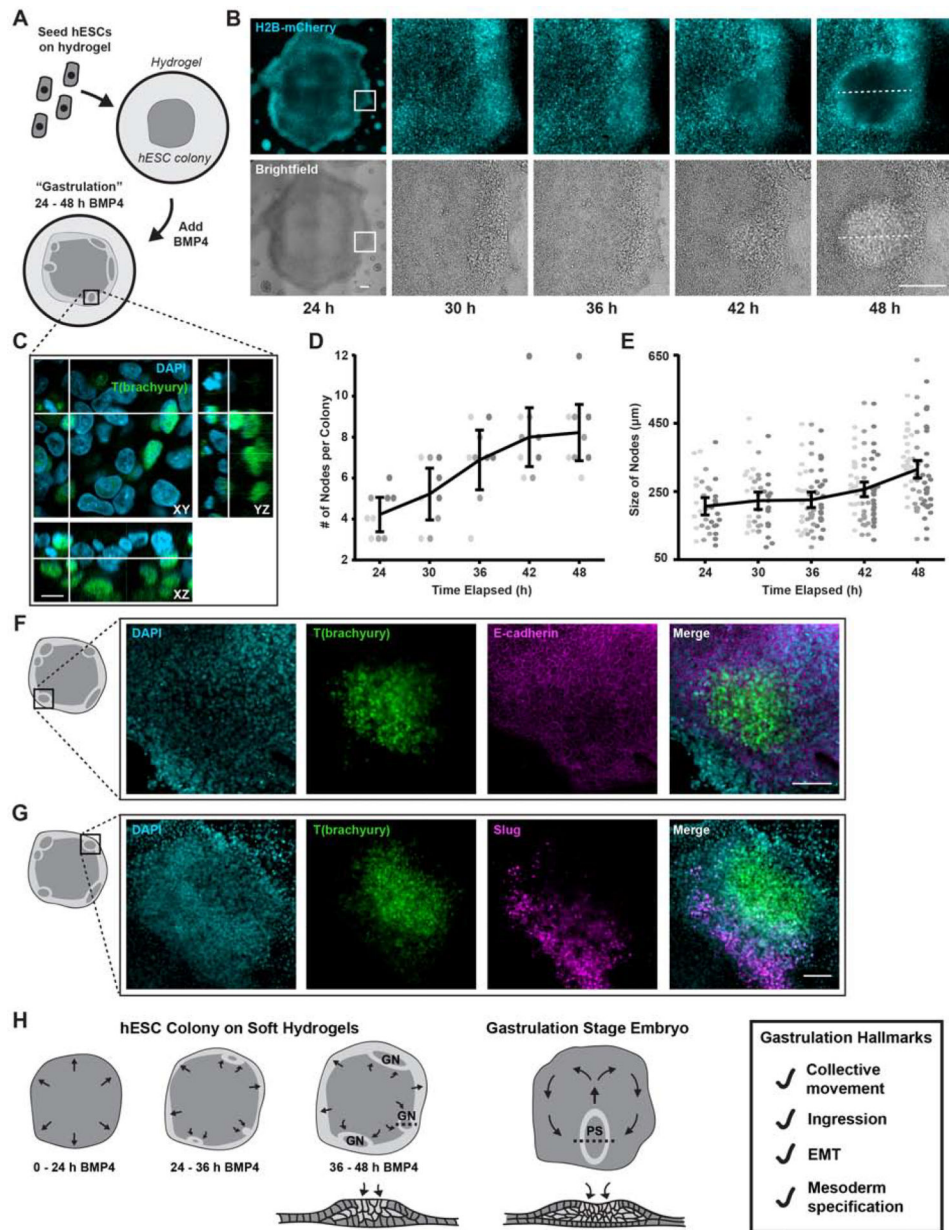


Figure 1: Compliant substrates promote hESC self-organization into "gastrulation-like" nodes.

(A) Cartoon of hESCs seeded on compliant (2,700 Pa) hydrogels and stimulated with BMP4.

(B) Representative time-lapse images of hESC colonies stimulated with BMP4. White rectangles indicate the region shown magnified in subsequent panels. Dashed lines indicate node size measurement, as plotted in (E). Scale bars = 250 μm .

(C) Representative Z-stack reconstruction of a "gastrulation-like" node after 48 h BMP4. Rectangle in (A) indicates imaged region. Scale bar = 10 μm .

(D) Plot of the number of nodes formed between 24 and 48 h BMP4. $n = 9$ (3, 3, 3) colonies.

(E) Plot of node size between 24 and 48 h BMP4. The dashed lines in (B) indicate node size measurement. Data points represent the size of each node identified from $n = 9$ colonies (3, 3, 3).

(F) Representative images of T(brachyury) expression, E-cadherin, and composite in the “gastrulation-like” nodes at 48 h BMP4. Rectangle on colony cartoon indicates imaged region. Scale bar = 100 μm .

(G) Representative images of T(brachyury) expression, Slug, and composite in the “gastrulation-like” nodes at 48 h BMP4. Rectangle on colony cartoon indicates imaged region. Scale bar = 100 μm .

(H) Schematic of the “gastrulation-like” phenotype observed in hESC colonies on compliant hydrogels, compared to gastrulation in the embryo. Cross-sections along dashed lines depicted below. GN = gastrulation node. PS = primitive streak. EMT = epithelial to mesenchymal transition.

For (D), (E): Data from independent experiments represented by different shades of gray and line and bars represent mean \pm 95% CI.

See also Figure S1, Video S1.

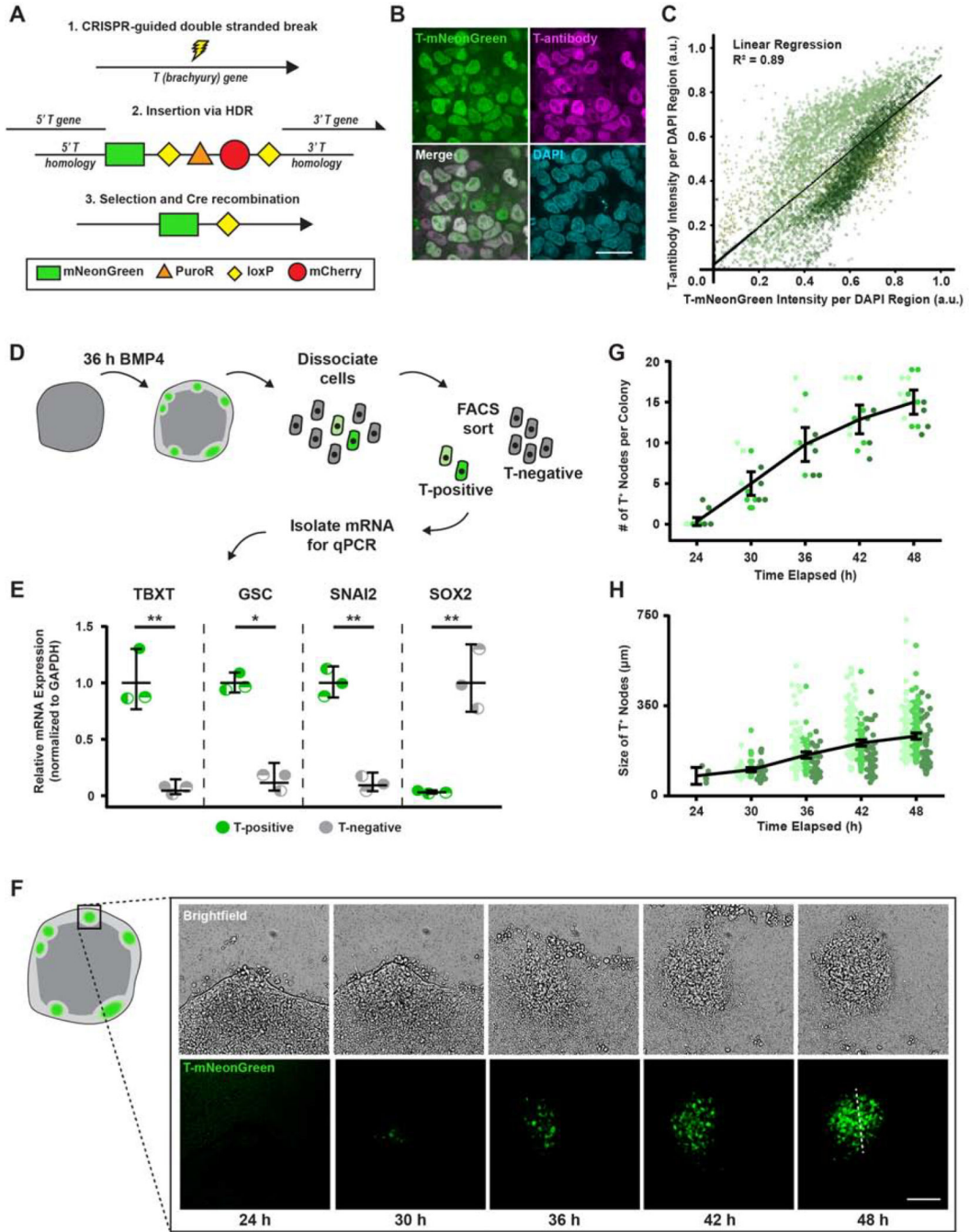


Figure 2: Real-time monitoring of hESC “gastrulation-like” nodes.

(A) Schematic representation of the T-mNeonGreen reporter system.

(B) Representative images of T(brachyury) labeled by the T-reporter, an antibody to T, and composite. Scale bar = 20 μ m.

(C) Plot of fluorescence intensity of T-mNeonGreen versus T-antibody per segmented nuclei. n = 33 (10, 13, 10).

(D) Cartoon of isolation protocol to compare gene expression between T-positive and T-negative cells.

(E) Relative mesoderm gene expression levels in T-positive and T-negative cells at 36 h BMP4.

(F) Representative time-lapse images of “gastrulation-like” nodes in the T-mNeonGreen reporter system. Rectangle on colony cartoon indicates imaged region. Dashed line indicates node size measurement, as plotted in (H). Scale bar = 100 μ m.

(G) Plot of the number of nodes formed between 24 and 48 h BMP4. n = 15 (5, 6, 4) colonies.

(H) Plot of node size between 24 and 48 h BMP4. The dashed line in (F) indicates node size measurement. Data points represent the size of each node identified from n = 15 (5, 6, 4) colonies.

For (C), (G), (H): Data from independent experiments represented by different shades of green.

For (E), (G), (H): Line and bars represent mean \pm 95% CI. HDR = homology-directed repair. a.u. = arbitrary units. TBXT = T-Box Transcription Factor T. GSC = goosecoid. *p < 0.05 and **p < 0.01.

See also Figure S2, Videos S2–S4.

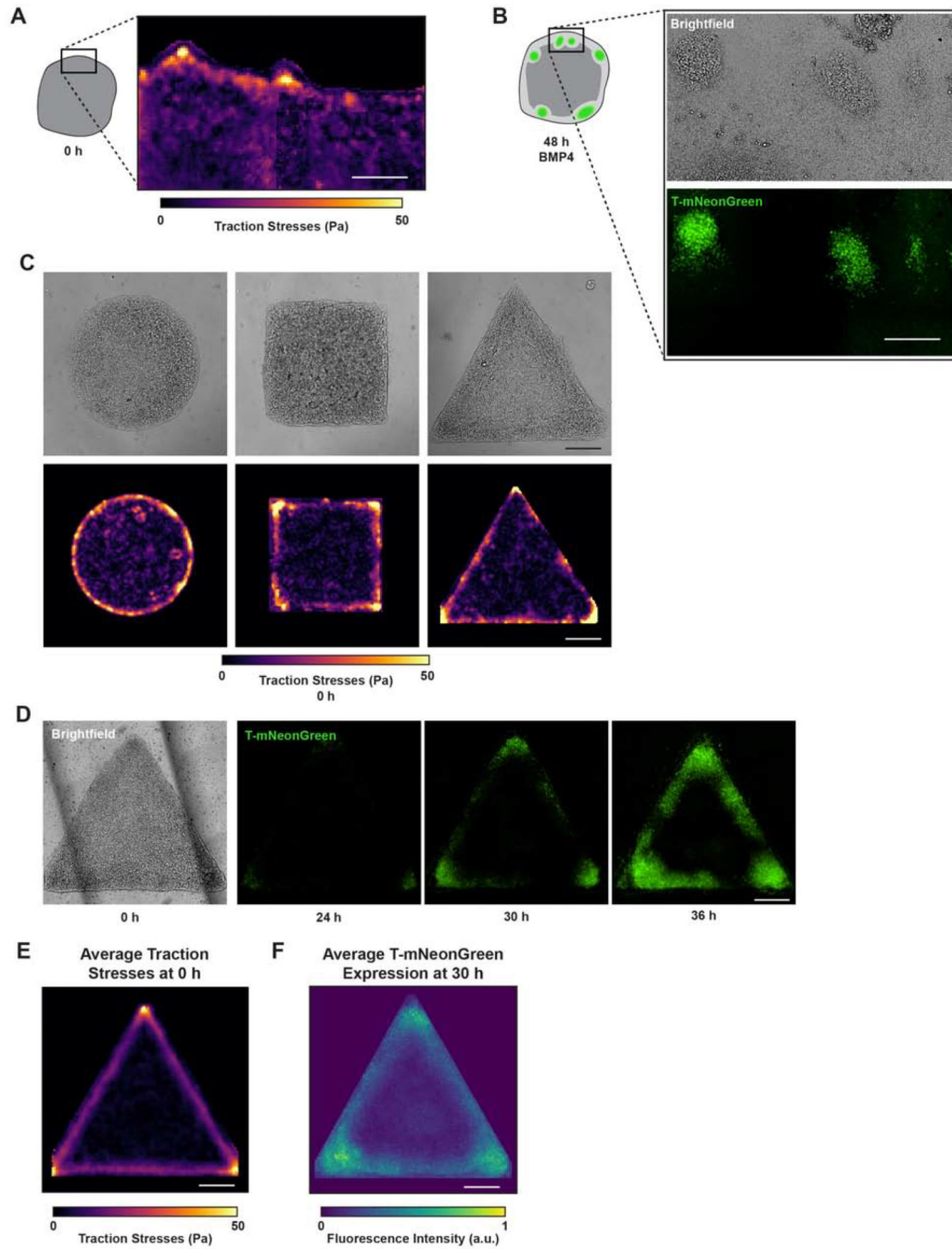


Figure 3: Cell-adhesion tension directs “gastrulation-like” node organization to specify mesoderm.

(A) Representative traction stress map of the periphery of unconfined hESC colonies prior to BMP4 stimulation. Rectangle on colony cartoon indicates measured region.

(B) Brightfield and T-mNeonGreen images 48 h after BMP4 in the same field of view where traction stresses were measured in (A).

(C) Representative brightfield images and corresponding traction stress maps measured for geometrically-confined hESC colonies on compliant gels before BMP4.

(D) Representative brightfield and time-lapse images of T-mNeonGreen expression for triangle hESC colonies on compliant gels following BMP4 addition.

(E) Map of average traction stresses measured for triangle hESC colonies before BMP4. $n = 19$ (3, 10, 6) colonies.

(F) Normalized average intensity map of T-mNeonGreen expression within triangle hESC colonies at 30 h BMP4. $n = 12$ (3, 1, 7, 1) colonies.

All scale bars = 250 μm . Pa = Pascals. a.u. = arbitrary units.

See also Figures S3–S4, Video S5.

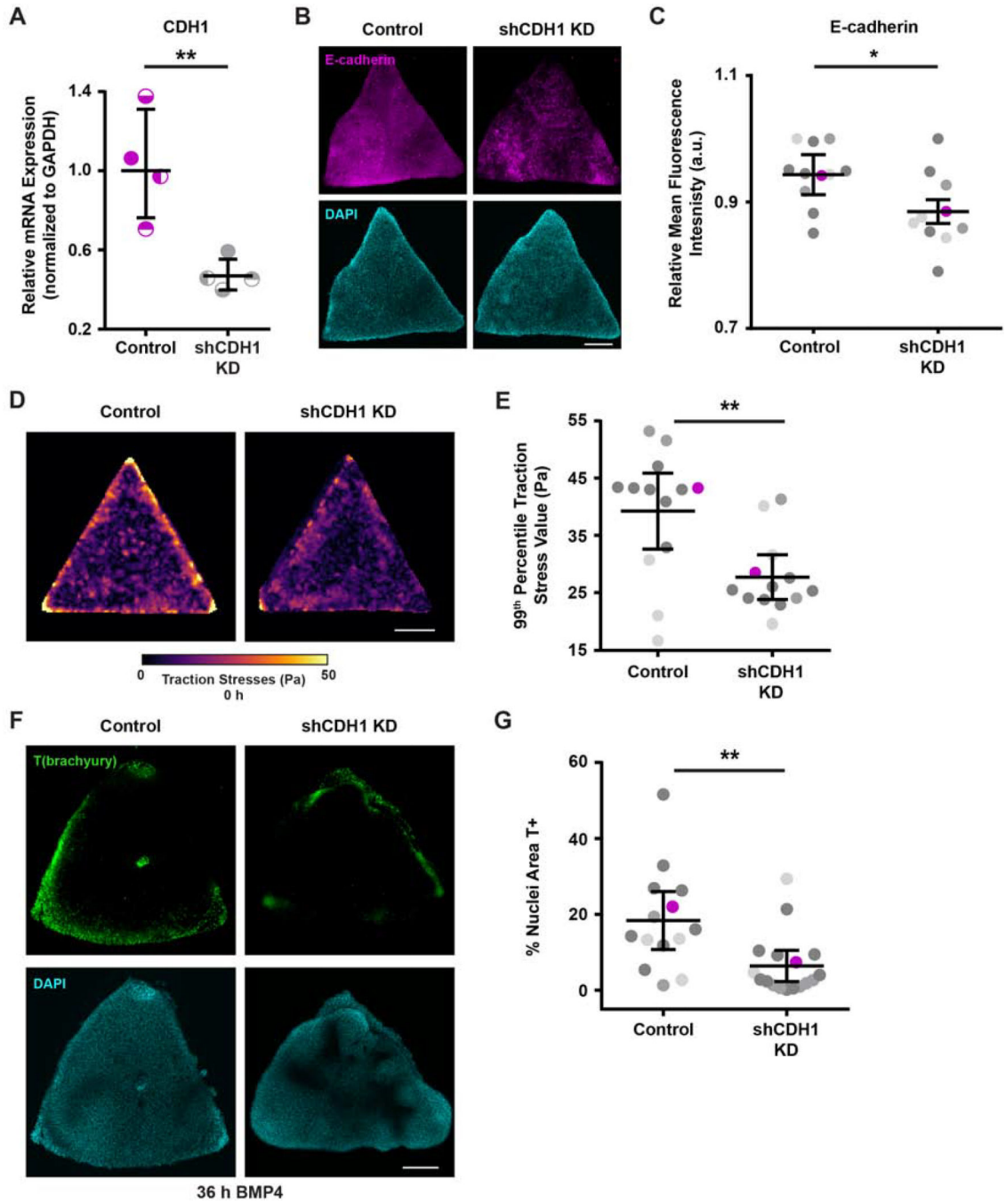


Figure 4: Cell-cell adhesion mediates the high tension required to develop “gastrulation-like” nodes.

(A) Relative CDH1 mRNA expression with and without shCDH1 knockdown.

(B) Representative images of E-cadherin expression with and without shCDH1 knockdown.

(C) Plot of relative E-cadherin mean fluorescence intensity with and without shCDH1 knockdown. Magenta data points correspond to the images shown in (B). n = 11 (2, 2, 7) control colonies and n = 10 (3, 2, 5) knockdown colonies.

(D) Representative traction stress maps for triangle hESC colonies with and without shCDH1 knockdown.

(E) Plot of the 99th percentile traction stress values from maps of triangle hESC colonies with and without shCDH1 knockdown. n = 13 (3, 2, 8) colony maps. Magenta data points correspond to representative maps in (D).

(F) Representative images of T(brachyury) expression at 36 h BMP4 in triangle colonies with and without shCDH1 knockdown.

(G) Plot of the % of nuclear area marked T-positive in triangle colonies with and without shCDH1 knockdown at 36 h BMP4. Magenta data points correspond to the images shown in (F). n = 14 (3, 3, 8) control colonies and n = 17 (2, 6, 9) knockdown colonies.

For (A), (C), (E), (G): Line and bars represent mean \pm 95% CI. For (C), (E), (G): Data from independent experiments represented by different shades of gray. All scale bars = 250 μ m. KD = knockdown. Pa = Pascals. a.u. = arbitrary units. *p < 0.05 and **p < 0.01. See also Figure S5.

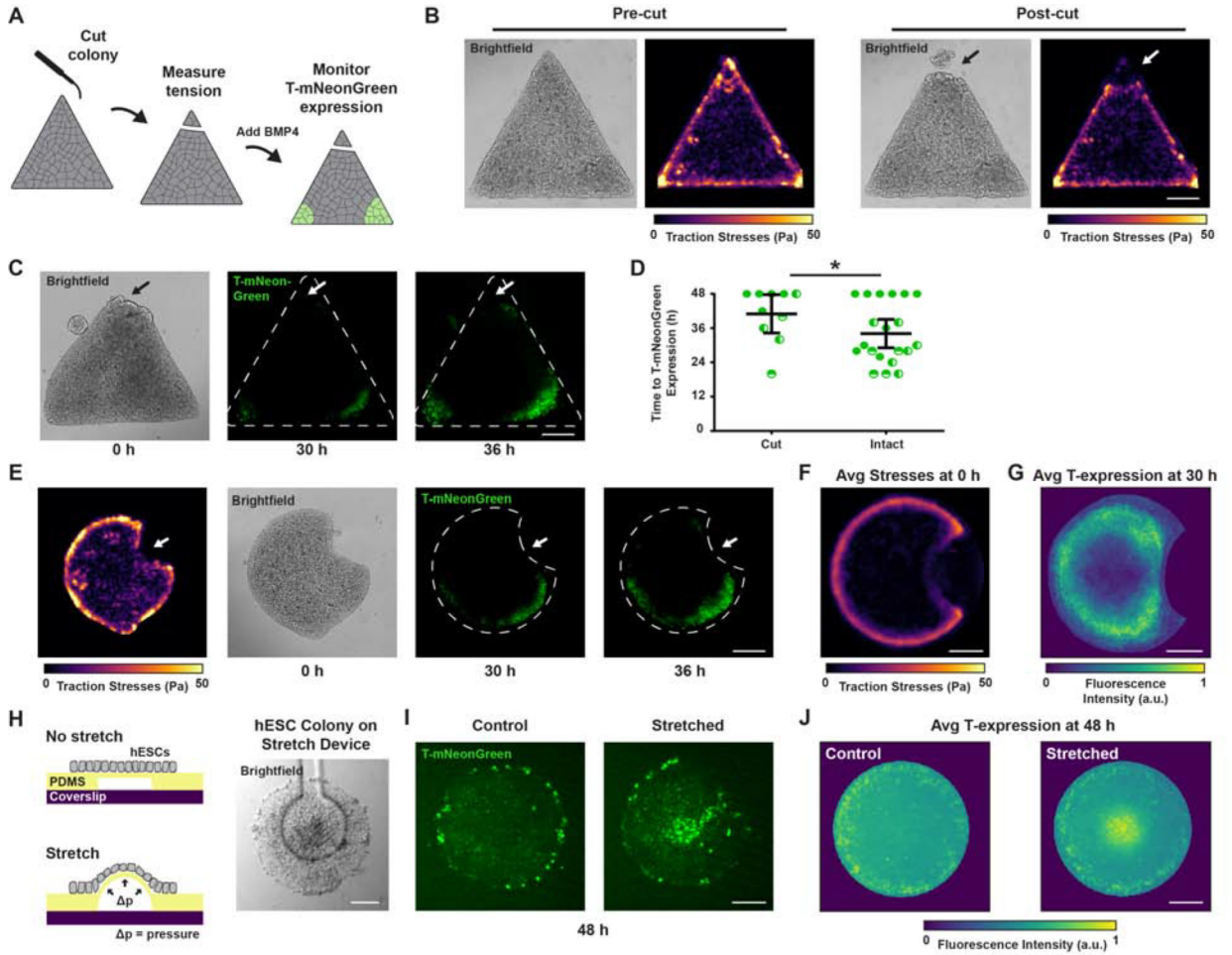


Figure 5: Ablating regions of high cell-adhesion tension inhibits, whereas mechanical stretching promotes mesoderm specification.

(A) Cartoon of eyebrow knife experiment.

(B) Representative brightfield images and traction stress maps before and after eyebrow knife ablation.

(C) Representative brightfield and time-lapse images of T-mNeonGreen expression following BMP4 stimulation for triangle hESC colonies with one corner ablated using the eyebrow knife prior to BMP4 addition. Arrow indicates site of eyebrow knife ablation.

(D) Plot of time to T-mNeonGreen expression in the corners of triangle hESC colonies with and without eyebrow knife ablation. Line and bars represent mean \pm 95% CI for n = 10 (2, 5, 3) colonies.

(E) Representative traction stress map prior to BMP4 addition and corresponding time-lapse images of T-mNeonGreen expression following BMP4 stimulation for Pac-Man hESC colonies. Arrow indicates concave edge (“mouth”) of Pac-Man.

(F) Map of average traction stresses measured for Pac-Man hESC colonies. n = 20 (3, 10, 4, 3) colonies.

(G) Normalized average intensity map of T-mNeonGreen expression within Pac-Man hESC colonies at 30 h BMP4. n = 20 (3, 10, 4, 3) colonies.

(H) Cartoon of mechanical stretching experiment and representative brightfield image of an hESC colony cultured on the stretching device.

(I) Representative images of T-mNeonGreen expression for hESC colonies with and without mechanical stretching during 48 h BMP4.

(J) Normalized average intensity maps of T-mNeonGreen expression for hESC colonies with and without mechanical stretching during 48 h BMP4. $n = 27$ (12, 8, 7) stretched colonies and $n = 39$ (21, 10, 8) control colonies.

For (A)-(G): Scale bars = 250 μm . For (H)-(J): Scale bars = 100 μm . Pa = Pascals. Avg = average. a.u. = arbitrary units. * $p < 0.05$.

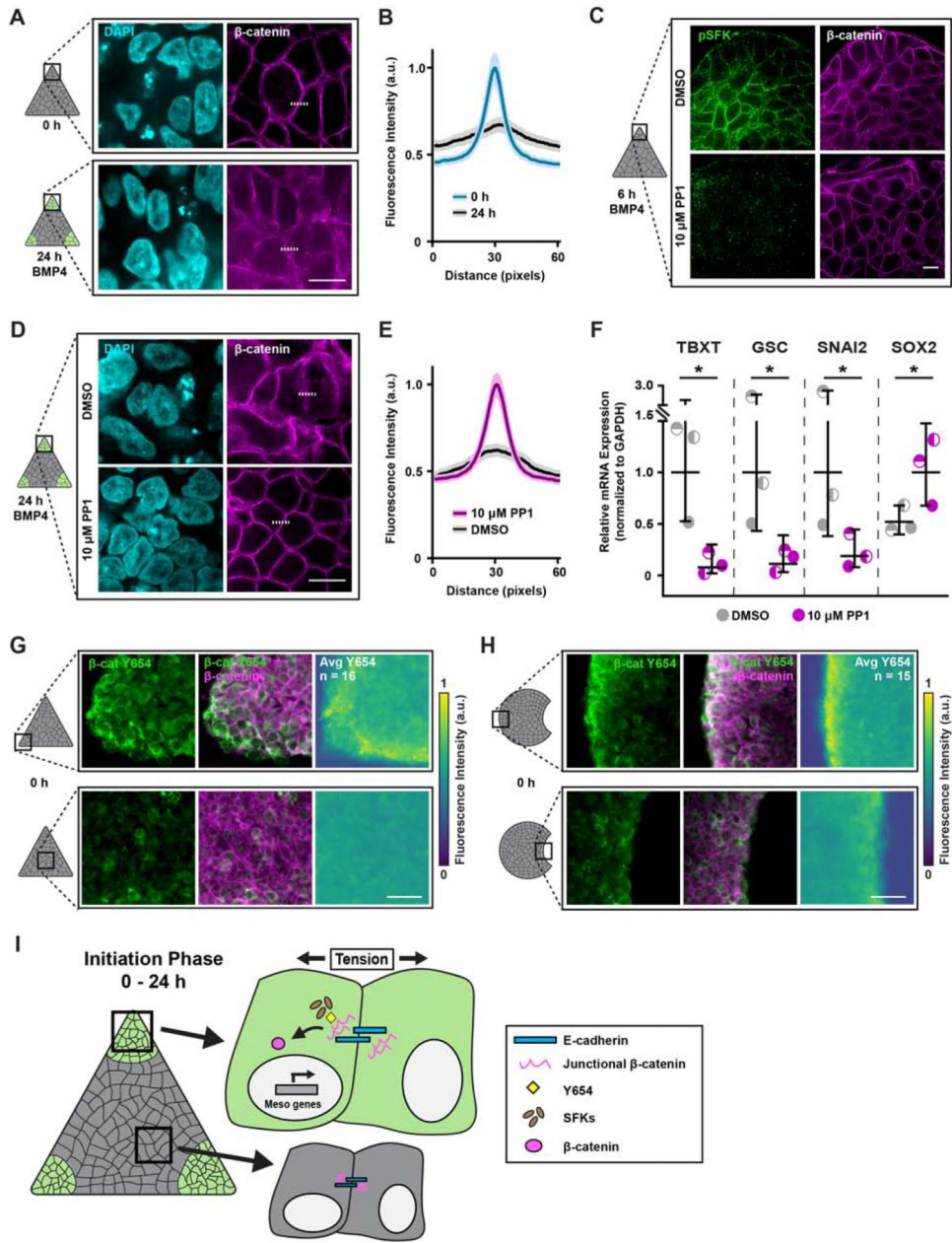


Figure 6: High tension promotes β -catenin release from adherens junctions to specify mesoderm. (A) Representative images of β -catenin expression in the corners of triangle hESC colonies before and 24 h after BMP4.

(B) Plot of mean (solid line) \pm 95% CI (shaded regions) fluorescence intensity of β -catenin at cell junctions in the corners of triangle hESC colonies before and 24 h after BMP4 stimulation. Dashed lines in (A) indicate plotted fluorescence intensity profiles. N = 130 profiles per condition from n = 26 (9, 8, 9) imaged colony corner ROIs.

(C) Representative images of phosphorylated Src-family kinase (pSFK) and β -catenin expression in the corners of triangle hESC colonies after 6 h BMP4 plus vehicle (DMSO) or Src inhibitor (PP1; 10 μ M).

(D) Representative images of β -catenin expression in the corners of triangle hESC colonies after 24 h BMP4 plus vehicle (DMSO) or Src inhibitor (PP1; 10 μ M).

(E) Plot of mean (solid line) \pm 95% CI (shaded regions) fluorescence intensity of β -catenin at cell junctions in the corners of triangle hESC colonies after 24 h BMP4 plus vehicle (DMSO) or Src inhibitor (PP1; 10 μ M). Dashed lines in (D) indicate plotted fluorescence intensity profiles. N = 130 profiles per condition from n = 26 (9, 8, 9) imaged colony corner ROIs.

(F) Relative mesoderm gene expression levels after 36 h BMP4 plus vehicle (DMSO) or Src inhibitor (PP1; 10 μ M). Line and bars represent mean \pm 95% CI.

(G) Representative images of β -catenin Y654 (green; left), composite β -catenin Y654 and normal β -catenin (merge; middle), and normalized average intensity map of β -catenin Y654 expression (right) within triangle hESC colonies prior to BMP4. n = 16 (3, 7, 6) colonies.

(H) Representative images of β -catenin Y654 (green; left), composite β -catenin Y654 and normal β -catenin (merge; middle), and normalized average intensity map of β -catenin Y654 expression (right) within Pac-Man hESC colonies prior to BMP4. n = 15 (5, 5, 5) colonies.

(I) Cartoon summarizing the mechanism by which regionally-localized high cell-adhesion tension exposes β -catenin Y654 to facilitate its phosphorylation and subsequent release, mediated by pSFKs, upon BMP4 stimulation.

For (A), (C), (D): Scale bars = 10 μ m. For (G), (H): Scale bars = 50 μ m. Rectangles on colony cartoons indicate imaged regions. β -cat Y654 = tyrosine 654 of β -catenin. pSFK = phosphorylated Src-family kinases. TBXT = T-Box Transcription Factor T. GSC = goosecoid. a.u. = arbitrary units. Avg = average. *p < 0.05.

See also Figure S6.

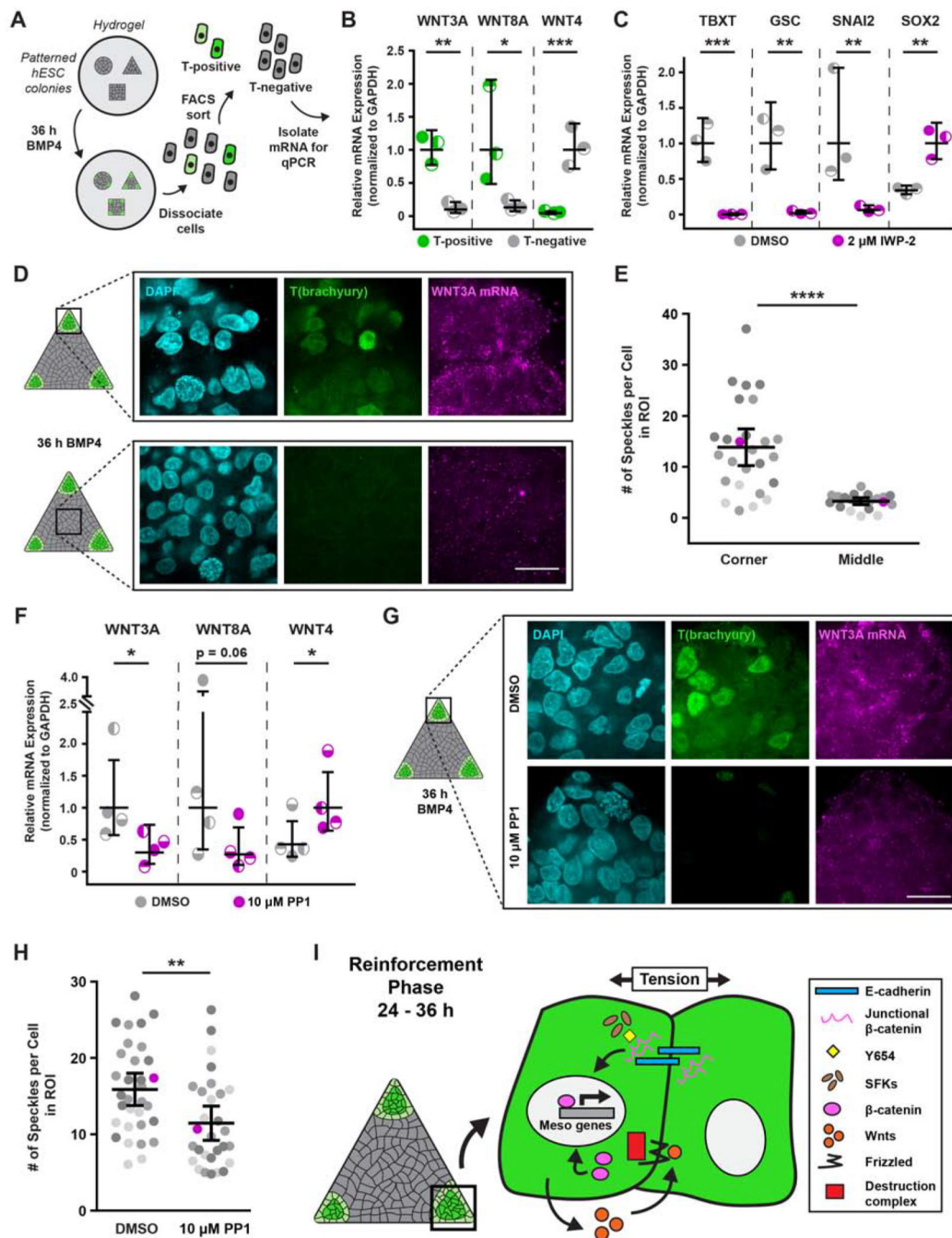


Figure 7: Wnt signaling reinforces mesoderm specification in regions of high tension.

(A) Cartoon of isolation protocol to compare Wnt ligand expression between T-positive and T-negative cells.

(B) Relative Wnt ligand expression levels in T-positive and T-negative hESCs after 36 h BMP4.

(C) Relative mesoderm gene expression levels after 36 h BMP4 plus vehicle (DMSO) or Wnt inhibitor (IWP-2; 2 μ M).

- (D)** Representative images of T(brachyury) protein expression and *in-situ*-detected WNT3A mRNA in the corner and middle of triangle hESC colonies after 36 h BMP4.
- (E)** Plot of *in-situ*-detected WNT3A speckles in the corner and middle of hESC colonies after 36 h BMP4. Magenta data points correspond to images shown in (D). n = 26 (4, 12, 10) imaged corner ROIs and n = 20 (3, 8, 9) imaged middle ROIs.
- (F)** Relative Wnt ligand expression levels after 36 h BMP4 plus vehicle (DMSO) or Src inhibitor (PP1; 10 μ M).
- (G)** Images of T(brachyury) protein expression and *in-situ*-detected WNT3A mRNA in the corners of triangle hESC colonies after 36 h BMP4 plus vehicle (DMSO; top) or Src inhibitor (PP1; 10 μ M; bottom).
- (H)** Plot of *in-situ*-detected WNT3A speckles in the corners of triangle hESC colonies after 36 h BMP4 plus vehicle (DMSO) or Src inhibitor (PP1; 10 μ M). Magenta data points correspond to images in (G). n = 26 (4, 12, 10) imaged ROIs from DMSO condition and n = 20 (3, 8, 9) imaged ROIs from PP1 condition.
- (I)** Cartoon summarizing the mechanism by which regions of high cell-adhesion tension direct mesoderm specification. The Src-mediated release of junctional β -catenin feeds forward and upregulates Wnt ligand expression to promote mesoderm specification. For (B), (C), (E), (F), (H): Line and bars represent mean \pm 95% CI. For (E), (H): Data from independent experiments represented by different shades of gray. Rectangles on colony cartoons indicate imaged regions. All scale bars = 20 μ m. *p < 0.05, **p < 0.01, ***p < 0.001, and ****p < 0.0001. See also Figure S7.

KEY RESOURCES TABLE

REAGENT or RESOURCE	SOURCE	IDENTIFIER
Antibodies		
Goat polyclonal anti-T(brachyury)	R&D Systems	Cat# AF2085; RRID: AB_2200235
Rabbit monoclonal anti-E-cadherin (24E10)	Cell Signaling Technology	Cat# 3195; RRID: AB_2291471
Rabbit monoclonal anti-Slug (C19G7)	Cell Signaling Technology	Cat# 9585; RRID: AB_2239535
Mouse monoclonal anti-Fibronectin (2F12)	Abcam	Cat# ab25583; RRID: AB_470662
Rabbit polyclonal anti- β -catenin-Y654	Sigma	Cat# SAB4300586; RRID: AB_10623284
Rabbit monoclonal anti- β -catenin (D10A8)	Cell Signaling Technology	Cat# 8480; RRID: AB_11127855
Mouse monoclonal anti- β -catenin (M1181)	ECM Biosciences	Cat# CM1181
Rabbit monoclonal anti-phospho-Src Family (Tyr416) (D49G4)	Cell Signaling Technology	Cat# 6943; RRID: AB_10013641
Rabbit polyclonal anti-POU5F1 (H-134)	Santa Cruz Biotechnology	Cat# sc-9081; RRID: AB_2167703
DAPI	Invitrogen	Cat# D3571; RRID: AB_2307445
Alexa Fluor 488 goat anti-mouse IgG	Abcam	Cat# ab150113; RRID: AB_2576208
Alexa Fluor 568 goat anti-mouse IgG	Abcam	Cat# ab175473
Alexa Fluor 488 goat anti-rabbit IgG	Abcam	Cat# ab150077; RRID: AB_2630356
Alexa Fluor 568 goat anti-rabbit IgG	Abcam	Cat# ab175471; RRID: AB_2576207
Alexa Fluor 488 donkey anti-goat IgG	Abcam	Cat# ab150129; RRID: AB_2687506
Bacterial and Virus Strains		
pX330-U6-Chimeric_BB-CBh-hSpCas9	Cong, L. et al. 2013.	Addgene plasmid# 42230; RRID: Addgene_42230
pBluescript II KS+	Stratagene	N/A
pLKO.1 neo	Unpublished, Laboratory of Sheila Stewart, Washington University in St. Louis	Addgene plasmid# 13425; RRID: Addgene_13425
pMD2.G envelope vector	Unpublished, Laboratory of Didier Trono, Swiss Federal Institute of Technology Lausanne (EPFL)	Addgene plasmid# 12259; RRID: Addgene_12259
psPAX2 packaging vector	Unpublished, Laboratory of Didier Trono, Swiss Federal Institute of Technology Lausanne (EPFL)	Addgene plasmid# 12260; RRID: Addgene_12260
Chemicals, Peptides, and Recombinant Proteins		
2-Hydroxy-4'-(2-hydroxyethoxy)-2methylpropiophenone (Irgacure D-2959)	Sigma	Cat# 410896; CAS: 106797-53-9
2% bis-acrylamide solution	BioRad	Cat# 1610142
40% acrylamide solution	BioRad	Cat# 1610140
Cultrex Basement Membrane Extract, Type 2, Pathclear (rBM; Matrigel equivalent)	R&D Systems	Cat# 3532-005-02
Cultrex Human Vitronectin, Pathclear	Trevigen	Cat# 3421-001-01
Denhardt's solution, 50x	Sigma	Cat# D2532
Dextran sulfate, avg M_w >500,000	Sigma	Cat# D8906; CAS: 9011-18-1
Diethyl pyrocarbonate (DEPC)	Sigma	Cat# D5758; CAS: 1609-47-8

REAGENT or RESOURCE	SOURCE	IDENTIFIER
Di(trimethylolpropane) tetraacrylate	Sigma	Cat# 408360; CAS: 94108-97-1
Formamide	Sigma	Cat# 11814320001; CAS: 75-12-7
G-418	Sigma	Cat# 4727878001; CAS: 108321-42-2
Glutaraldehyde, 70% aqueous	Electron Microscopy Sciences	Cat# 16350
Heparin sodium salt from porcine intestinal mucosa	Sigma	Cat# H3393; CAS: 9041-08-1
Isopropyl- β -D-thiogalactoside (IPTG)	Sigma	Cat# 10724815001; CAS: 367-93-1
IWP-2 (Wnt processing and secretion inhibitor)	MedChem Express	Cat# HY-13912; CAS: 686770-61-6
M-MLV Reverse Transcriptase	BioChain	Cat# Z5040002
Norland Optical Adhesive 74 (NOA-74)	Norland Products, Inc.	Cat# NOA74
N-succinimidyl acrylamido hexanoic acid (N6)	Lakins, J.N. et al. 2012	N/A
Polydimethylsiloxane (PDMS), SYLGARD™ 184 Silicone Elastomer Kit	Dow	Cat# 4019862
Polyethylenimine, branched (PEI)	Sigma	Cat# 408719; CAS: 25987-06-8
Potassium persulfate	Sigma	Cat# 216224; CAS: 7727-21-1
PPI (Src inhibitor)	Sigma	Cat# 567809; CAS: 172889-26-8
Recombinant human FGF-basic (bFGF, 154 a.a.)	PeproTech	Cat# 100-18B
Recombinant human BMP-4	PeproTech	Cat# 120-05ET
Ribonucleoside vanadyl complexes	Sigma	Cat# R3380
SU-8 3050 negative photoresist	Kayaku Advanced Materials, Inc.	Cat# SU-8 3000
TEMED (N,N,N',N'-tetramethylethylenediamine)	BioRad	Cat# 161-0800
Tth DNA Polymerase	Sigma	Cat# 11480022001
Vent DNA Polymerase	New England BioLabs, Inc.	Cat# M0254S
Y-27632 dihydrochloride (ROCK inhibitor)	Tocris	Cat# 1254
Critical Commercial Assays		
PerfeCTa SYBR Green FastMix	Quantabio	Cat# 95072-05K
Surveyor Assay	Transgenomics	Cat# 706020
TRIzol	Invitrogen	Cat# 15596-018
Experimental Models: Cell Lines		
Human: H9 ES cell line	Laboratory of Susan Fisher, University of California San Francisco	N/A
Human: H2B-mCherry H9 cell line	This manuscript	N/A
Human: shCDH1 H9 cell line	This manuscript	N/A
Human: T-mNeonGreen H9 cell line	This manuscript	N/A
Human: Human embryonic kidney (HEK) 293T cell line	Laboratory of Warren Pear, University of Pennsylvania	N/A
Mouse: Mouse embryonic fibroblasts (MEFs), derived from CF-1 mice	Laboratory of Susan Fisher, University of California San Francisco	N/A
Oligonucleotides		

REAGENT or RESOURCE	SOURCE	IDENTIFIER
Guide RNA for Cas9 targeting to TBXT gene: 5' - GCCTTGCTGCTTCACATGGA - 3'	This manuscript	N/A
Short hairpin for CDH1 knockdown: 5' - GAACGAGGCTAACGTCGTAAT - 3'	Przybyla, L. et al. 2016b	N/A
qPCR primers: See Table S1	Integrated DNA Technologies	N/A
Random Hexamers	Applied Biosystems	Cat# N8080127
Split initiator hybridization probes: See Table S2	Integrated DNA Technologies	N/A
Software and Algorithms		
CellProfiler 3.1.9 or later	McQuin, C. et al. 2018	https://cellprofiler.org
Elveflow Smart Interface Software	Elveflow	https://www.elveflow.com/microfluidicproducts
FIJI (ImageJ 1.52a or later, running on Java 1.8.0_172 or later)	Schindelin, J. et al. 2012	https://imagej.net/Fiji
FTTC plugin for FIJI	Tseng, Q. et al. 2012	https://sites.google.com/site/qingzongtseng/tfm
ilastik 1.3.3	Berg, S. et al. 2019	https://www.ilastik.org
Imaris 9.2	Oxford Instruments	https://imaris.oxinst.com
Jython 2.7.2	Jython	https://www.jython.org
MATLAB R2018b or later	MathWorks	https://www.mathworks.com/products/matlab.html
Perceptually uniform colormap functions for MATLAB	Biguri, A. 2020. MATLAB Central File Exchange	https://www.mathworks.com/matlabcentral/fileexchange/51986-perceptuallyuniform-colormaps
PIV plugin for FIJI	Tseng, Q. et al. 2012	https://sites.google.com/site/qingzongtseng/piv
Prism 6	GraphPad	https://www.graphpad.com/scientificsoftware/prism/
Python 3.8.5	Python	https://www.python.org/
Traction Force Microscopy analysis and visualization scripts	This manuscript	https://github.com/jmmuncie/TF_hESC
Other		
FluoSpheres™ carboxylate-modified microspheres, 1.0 μm, red fluorescent (580/605), 2% solids	Invitrogen	Cat# F8821